Rotation and stability of the circumnuclear gas disk in the Galactic Center potential by the ALMA CMZ Exploration Survey (ACES)

Yoshiaki SOFUE, [1,*] Steven N. LONGMORE, [2,3] Daniel WALKER, [4] Adam GINSBURG, [5] Jonathan D. HENSHAW, [2,6] John BALLY, [7] Ashley T. BARNES, [8] Cara BATTERSBY, [9] Laura COLZI, [10] Paul HO, [11] Izaskun JIMENEZ-SERRA, [10] J. M. Diederik KRUIJSSEN, [3] Elizabeth MILLS, [12] Maya A. PETKOVA, [13] Mattia C. SORMANI, [14] Jen WALLACE, [9] Jairo ARMIJOS-ABENDAÑO, [15] Zi-Xuan FENG, [14,16] Karl FITENI, [14,17] Pablo GARCÍA, [18,19] Savannah GRAMZE, [5] Christian HENKEL, [20] Pei-Ying HSIEH, [21] Ralf S. KLESSEN, [16,22] Francisco NOGUERAS-LARA, [23] Dylan M. PARÉ, [24] Victor M. RIVILLA, [10] and Álvaro SÁNCHEZ-MONGE [25,26]

[1] Institute of Astronomy, The University of Tokyo, 2-21-1 Osawa, Mitaka, Tokyo 181-0015, Japan
[2] Astrophysics Research Institute, Liverpool John Moores University, IC2, Liverpool Science Park, 146 Brownlow Hill, Liverpool L3 5RF, UK
[3] Cosmic Origins Of Life (COOL) Research DAO, Germany
[4] UK ALMA Regional Centre Node, Jodrell Bank Centre for Astrophysics, Oxford Road, The University of Manchester, Manchester M13 9PL, UK
[5] Department of Astronomy, University of Florida, P.O. Box 112055, Gainesville, FL 32611, USA
[6] Max Planck Institute for Astronomy, Königstuhl 17, D-69117 Heidelberg, Germany
[7] Center for Astrophysics and Space Astronomy, Department of Astrophysical and Planetary Sciences; University of Colorado, Boulder, CO 80389, USA
[8] European Southern Observatory (ESO), Karl-Schwarzschild-Strasse 2, D-85748 Garching, Germany
[9] Department of Physics, University of Connecticut, 196A Auditorium Road, Unit 3046, Storrs, CT 06269, USA
[10] Centro de Astrobiologia (CAB), CSIC-INTA, Carretera de Ajalvir km 4, Torrejon de Ardoz, 28850 Madrid, Spain
[11] AS/NTU Astronomy-Mathematics Building, Roosevelt Rd, Taipei 10617, Taiwan
[12] Department of Physics and Astronomy, University of Kansas, 1251 Wescoe Hall Drive, Lawrence, KS 66045, USA
[13] Space, Earth and Environment Department, Chalmers University of Technology, SE-412 96 Gothenburg, Sweden
[14] Como Lake centre for AstroPhysics (CLAP), DiSAT, Università dell'Insubria, via Valleggio 11, 22100 Como, Italy
[15] Observatorio Astronómico de Quito, Observatorio Nacional, Escuela Politécnica Nacional, Interior del Parque La Alameda, 170136, Quito, Ecuador
[16] Universität Heidelberg, Zentrum für Astronomie, Institut für Theoretische Astrophysik, Albert-Ueberle-Str. 2, 69120 Heidelberg, Germany
[17] Institute of Space Sciences & Astronomy, University of Malta, Msida MSD 2080, Malta
[18] Chinese Academy of Sciences South America Center for Astronomy, National Astronomical Observatories, CAS, Beijing 100101, China
[19] Instituto de Astronomía, Universidad Católica del Norte, Av. Angamos 0610, Antofagasta, Chile
[20] Max-Planck-Institut für Radioastronomie, Auf dem Hügel 69, Bonn, Germany
[21] National Astronomical Observatory of Japan, 2-21-1 Osawa, Mitaka, Tokyo 181-8588, Japan
[22] Universität Heidelberg, Interdisziplinäres Zentrum für Wissenschaftliches Rechnen, Im Neuenheimer Feld 225, 69120 Heidelberg, Germany
[23] Instituto de Astrofísica de Andalucía (CSIC), Glorieta de la Astronomía s/n, E-18008 Granada, Spain
[24] Joint ALMA Observatory, Alonso de Cordova 3107, Vitacura, Casilla 19001, Santiago de Chile, Chile
[25] Institut de Ciències de l'Espai (ICE), CSIC, Campus UAB, Carrer de Can Magrans s/n, E-08193 Bellaterra, Barcelona, Spain
[26] Institut d'Estudis Espacials de Catalunya (IEEC), E-08860 Castelldefels, Barcelona, Spain
*E-mail: sofue@ioa.s.u-tokyo.ac.jp

Abstract

We investigated the gravitational potential and mass distribution in the Galactic Center by examining the morphology and kinematics of the circumnuclear gaseous disk revealed by the molecular line data from the ALMA CMZ Exploration Survey. We obtain an estimate of the shape of the potential within the central $\sim$20 pc to reproduce the observed properties of the circumnuclear gas disk by simulating the motion of test particles for various axial ratios and show that the potential is approximately spherical. We construct a rotation curve by applying the terminal velocity method to the position–velocity diagrams, and calculate the mass distribution in the Galactic Center. The distribution of mass density is found to be of cusp type, approximated by $\rho_{\rm dyn} \sim 1.56 \times 10^5 (R/1\,{\rm pc})^{-1.9}\ M_\odot\ {\rm pc}^{-3}$, where R is the distance from the nucleus. We discuss the tidal effect caused by the gravitational potential that produces the rotation curve and show that the gas disk is stable against self-gravitational contraction within a critical radius of $R_{\rm T} \sim 14\ (\rho_{\rm gas}/10^5 {\rm H}_2\ {\rm cm}^{-3})^{-1/2}$ pc. This suggests suppression of star formation and a top-heavy initial mass function in the circumnuclear region.

Keywords: Galaxy: center — Galaxy: structure — ISM: clouds — ISM: kinematics and dynamics — stars: formation

1 Introduction

The central molecular zone (CMZ) of our Galaxy is a high-density molecular gas disk with moderate star formation (Henshaw et al. 2016, 2023; Sofue 2022; Battersby et al. 2025), which rotates in the deep gravitational potential of the Galactic bulge and the central supermassive black hole. Extensive studies of the kinematics of the CMZ have revealed a large-scale multi-arm structure (Sofue 1995, 2022) and/or a twisted ellipse structure (Molinari et al. 2011; Longmore et al. 2013; Kruijssen et al. 2015; Henshaw et al. 2016; Lipman et al. 2025). Recently, we (Sofue et al. 2025a, 2025b) showed that the inner CMZ is composed of several rotating arms and rings using the molecular line cube data taken by the large project ACES (ALMA CMZ Exploration Survey: Longmore et al. 2025; Ginsburg et al. 2025; Walker et al. 2025; Lu et al. 2025; Hsieh et al. 2025), where the kinematic properties of the molecular gas in the position–velocity diagrams (PVD) are shown to provide information about the gravitational potential in which it is orbiting.

ALMA observations have also provided detailed individual studies of the circumnuclear disk (CND: Hsieh et al. 2021). However, the innermost region within 20 pc around Sgr A*, one of the major parts of the CMZ, has not yet been thoroughly studied, and in fact multiple arm and ring structures have been recognized (Sofue et al. 2025a, 2025b). The high-resolution and high-sensitivity data from ACES with uniform mapping quality across the entire CMZ makes it possible to investigate these individual structures from a more general perspective.

The innermost region of the CMZ is known to be the CND identified as Arms V and VI in Sofue et al. (2025a), which are high-density molecular tori of radii ∼2 to ∼10 pc (Oka et al. 2011; Liu et al. 2012; Mills et al. 2013, 2017; Hsieh et al. 2017, 2021; Tsuboi et al. 2018). The CND exhibits two-fold dynamical properties which suggest that it is a torus that is being fueled from the outer arms of the CMZ and is fuelling the more inner region, including the nucleus and the minispiral (Paumard et al. 2004; Kunneriath et al. 2012; Liu et al. 2012; Moser et al. 2017; Tsuboi et al. 2016, 2017).

Extensive hydrodynamical simulations have been performed to study the evolution and gas dynamics in the Galactic Center (Kruijssen et al. 2015, 2019; Krumholz et al. 2017; Dale et al. 2019; Ridley et al. 2017; Tress et al. 2020; Hunter et al. 2024). In the current work, there are two types of density profiles that have been used to create the gravitational potential as listed below: (i) Plateau or finite-peak type density distribution as $\rho \propto 1/[1 + (R/a)^n]$ (Miyamoto & Nagai 1975) or $\rho \propto \exp[-b(R/a)^n]$ (Launhardt et al. 2002), where R is the radius from the nucleus, and a, b, and n are constants. (ii) Cusp type with infinite central density as $\rho \propto R^{-n}$ with $n = 2$ (Binney et al. 1991) or $n = 1$ (Navarro et al. 1997). In 2D or 3D treatments, the scale radii and height are taken as free parameters to represent the shape of the potential.

In order to construct a more realistic model to understand the CMZ, which is a gaseous disk orbiting in the gravitational potential, the determination of the underlying potential based on observations is crucial. The molecular line data of ACES, covering the entire CMZ from the nucleus to its edge at high angular and velocity resolutions, are ideal for this purpose. In this paper, our aim is to constrain the gravitational potential

of the GC region by analyzing the PVDs of the CS ($J = 2$–1), $H^{13}CN$ ($J = 1$–0), and H40α line data from ACES.

There are two approaches to study the potential or, equivalently, the mass distribution. One way is to measure the surface density distribution of stars using infrared photometry (Fritz et al. 2016; Nishiyama & Schödel 2013; Portail et al. 2017; Gallego-Cano et al. 2020). The other method is to measure the rotation curve (RC) of the gaseous disk and/or the velocity dispersion of the stars (Sofue & Rubin 2001; Sofue 2020). We adopted the RC method and applied it to the PVDs in the molecular and recombination lines of the CMZ taken from the ACES data cubes.

This paper is structured as follows. In section 2 we describe the kinematic properties of inner molecular disks, particularly the CND. In section 3 we perform test-particle simulations of the kinematical evolution of a molecular cloud and give a constraint on the shape of the potential, which will be shown as spherical. In section 4, we derive the terminal velocity (TV) curve of the CMZ using the longitude–velocity diagrams in the CS and H40α lines. In section 5 we calculate the dynamical mass distribution in the Galactic Center, assuming that the gravitational potential is nearly spherical in the entire CMZ. Section 6 is devoted to the analysis of stability and tidal effect on a molecular clump in the molecular disk with the observed rotation curve. In section 7 we comment on the implication of the results and the consistency with the current studies. We adopted a distance of $R_0 = 8.2$ kpc to the GC, close to a recent measurement (GRAVITY Collaboration 2019).

2 Data and maps

We describe the data and maps used in this paper.

2.1 Data

The molecular line cubes in this work were taken from the internal release version (2024 August and 2025 October) of the 12 m + 7 m + TP (Total Power) mode data from the ALMA Cycle 8 Large Program "ALMA Central Molecular Zone Exploration Survey" (ACES, 2021.1.00172.L: Longmore et al. 2025). ACES observed the CMZ in ALMA Band 3, covering a frequency range of ∼86–101 GHz in six spectral windows of varying spectral resolution and bandwidth. In this paper we use the lines CS ($J = 2$–1) (CS) and $H^{13}CN$ ($J = 1$–0) (HCN) to trace the dense molecular gas (Shirley 2015). The CS ($J = 2$–1) and $H^{13}CN$ ($J = 1$–0) line data at frequencies of 97.9810 and 86.3399 GHz have angular resolutions of 2″.21 and an rms noise of 0.004 Jy beam^{-1} (0.10 K) with velocity channel increments of 1.45 and 0.85 km s^{-1}, respectively. We also used the H40α line at 99.02295 GHz to trace the ionized gas of the minispiral in the innermost region around Sgr A* at the same angular resolution and a velocity resolution of 1.5 km s^{-1}. The intensity scales are in Jy beam^{-1}, and 1 Jy beam^{-1} = 26.1 and 22.2 K in the main-brightness temperature (T_B) at 98 and 86 GHz, respectively. In the present work, we cut out the innermost regions from the ACES cubes, which cover a region of the CMZ at $0°.6 \lesssim l \lesssim +0°.9$ and $-0°.3 \lesssim b \lesssim +0°.1$ with spatial and velocity grids of ($0″.5 \times 0″.5 \times 0.15$ km s^{-1}) (Longmore et al. 2025).

We mention that the CS ($J = 2$–1) line is typically a tracer that may be moderately optically thick. Linke and Goldsmith

(1980) find opacities of 0.3–3.0 in classical star-forming regions of the Galactic disk, while Humire et al. (2020) find values of 1.0–2.8 in Galactic center clouds. On the other hand, the H^{13}CN ($J = 1$–0) line is relatively optically thin (Liu et al. 2023). This property will be used to argue for the presence of the central hole in the CND in subsection 2.4.

2.2 Maps

Figure 1 shows the moment 0 (integrated intensity) and moment 1 (velocity field) maps of the CND on the CS ($J = 2$–1) and H^{13}CN ($J = 1$–0) lines. The CND draws an ellipse in the sky with the major axis at the position angle $PA \sim 70°$ and a minor-to-major axial ratio of $b/a \sim 0.2$. The ellipse is associated with several bifurcated arms trailing outward in the clockwise sense. The north-east part of the ring is missing due to absorption against the radio continuum of Sgr A, indicating that the upper side of the ring is on the near side of Sgr A* (Sofue et al. 2025a).

The interior of the ellipse at $R \lesssim 1.5$ pc makes a hole of a depth as low as ~ 3 mJy beam^{-1} km s^{-1}, which is more clearly revealed by a cross-section of the total intensity map along the Galactic plane through Sgr A* shown in figure 2. The sharp negative peak in the center is due to absorption against the continuum of Sgr A*.

The hole coincides positionally with the minispiral of the ionized hydrogen gas. The electron density has been measured to be $n_e \sim 6 \times 10^3$ cm^{-3} as inferred from observations of the H92α recombination-line (Zhao et al. 2009) and $\sim (7$–$13) \times 10^3$ cm^{-3} of the H42α line (Tsuboi et al. 2017). If a value of 10^4 H cm^{-3} is typical along the main minispiral arms, the total mass of ionized hydrogen amounts only to $\sim 10^2$ $M_\odot$ for three arms of 1.5 pc in length and 0.2 pc in width. This is two to three orders of magnitude smaller than the mass needed to fill the hole by molecular gas with a density comparable to that in the CND.

2.3 Position–velocity diagrams

In figure 3 we show the PVDs along the major axis of the CND at position angle 70° across Sgr A* in CS, HCN and H40α lines. In the appendix (figure 20) we show channel maps of the longitude– and latitude–velocity diagrams (LVD and BVD) in the CS ($J = 2$–1) line.

The CND is recognized as the broad tilted ridge in the LVD and PVD, obliquely crossing the horizontal ridges due to the fore- and background CMZ and Galactic disk. The LVD ridge has a mean velocity gradient of $dv/dl \sim 9000$ km s^{-1} deg^{-1}, as measured for Arm VI (CND) in Paper I, corresponding to a value for a radius ~ 2 pc ring rotating at ~ 120 km s^{-1}. The broad width of the LVD ridge indicates a significant non-circular motion of the CND. BVDs also show a similar property to LVDs, indicating a tilted ridge.

2.4 CND and central cavity

In our previous paper (Sofue et al. 2025b) we have shown that there are several arms in the CMZ, named Arms I to VII. The CND is Arm VI, which is associated with the high-speed cloud G+0.02−0.02 +100 km s^{-1} and forms the same family with a fainter but more coherent arm of radius 8 pc. Thus, the circumnuclear region is characterized by multiple rotating rings. The simulation in the previous section also applies to the 8–10 pc arm (ring) by taking the normalization length to
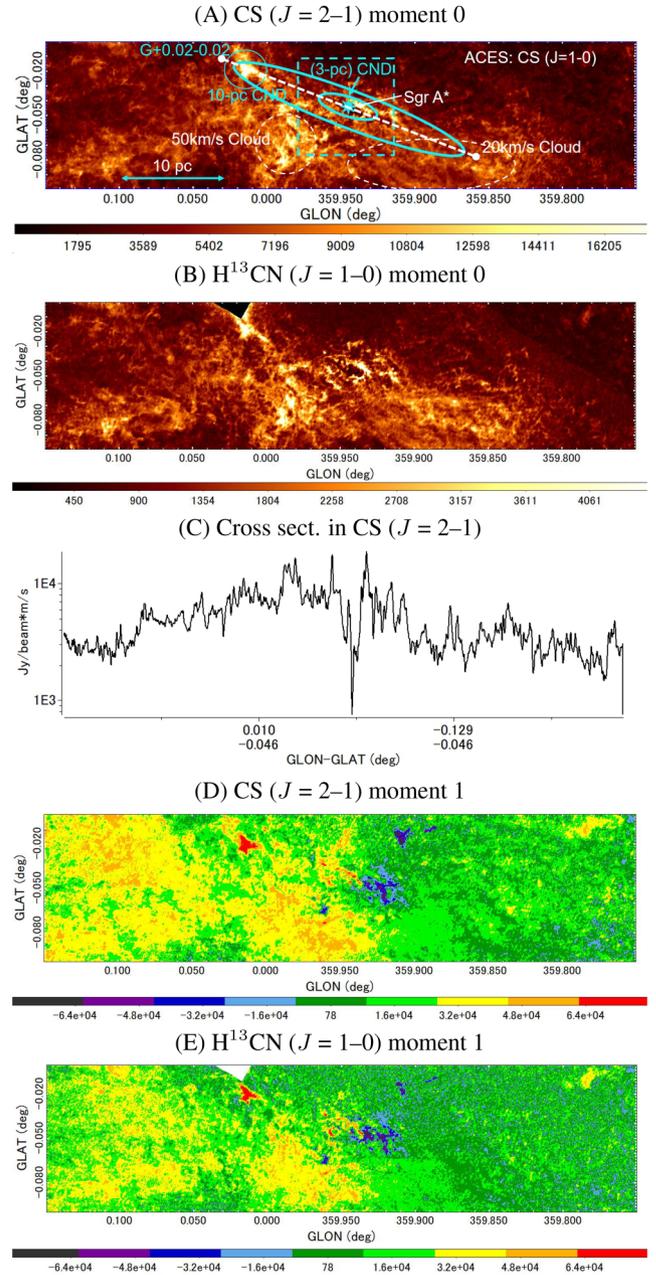

Fig. 1. (A) Moment 0 maps of the central 0°.4 × 0°.1 region around Sgr A* in the CS ($J = 2$–1) line by ACES. GLON and GLAT stand for l and b, respectively. The structures discussed in the paper are illustrated. (B) Same as (A), but in H^{13}CN ($J = 1$–0). (C) Longitudinal cross-section of CS ($J = 2$–1) moment 0 map across Sgr A*. Note the central hole inside the CND, which is enlarged in figure 2. The sharp negative peak is due to absorption of the continuum from Sgr A*. (D), (E) Moment 1 maps of CS ($J = 2$–1) and H^{13}CN ($J = 1$–0) lines, respectively, in units of m s^{-1}. Note the regular Galactic rotation with positive velocities at positive longitudes and negative velocities at negative longitudes.

~ 10 pc. Accordingly, a spherical potential is again preferred in order to keep the ring-like structure of Arm V.

The CND is defined as the massive molecular torus of several pc radius rotating around Sgr A* (Oka et al. 2011; Mills et al. 2017; Tsuboi et al. 2018; Hsieh et al. 2021). The torus feature can be clearly recognized by the central hole on the moment 0 map, as shown by the moment 0 map and the cross-section of the intensity in figure 2. The feature is naturally
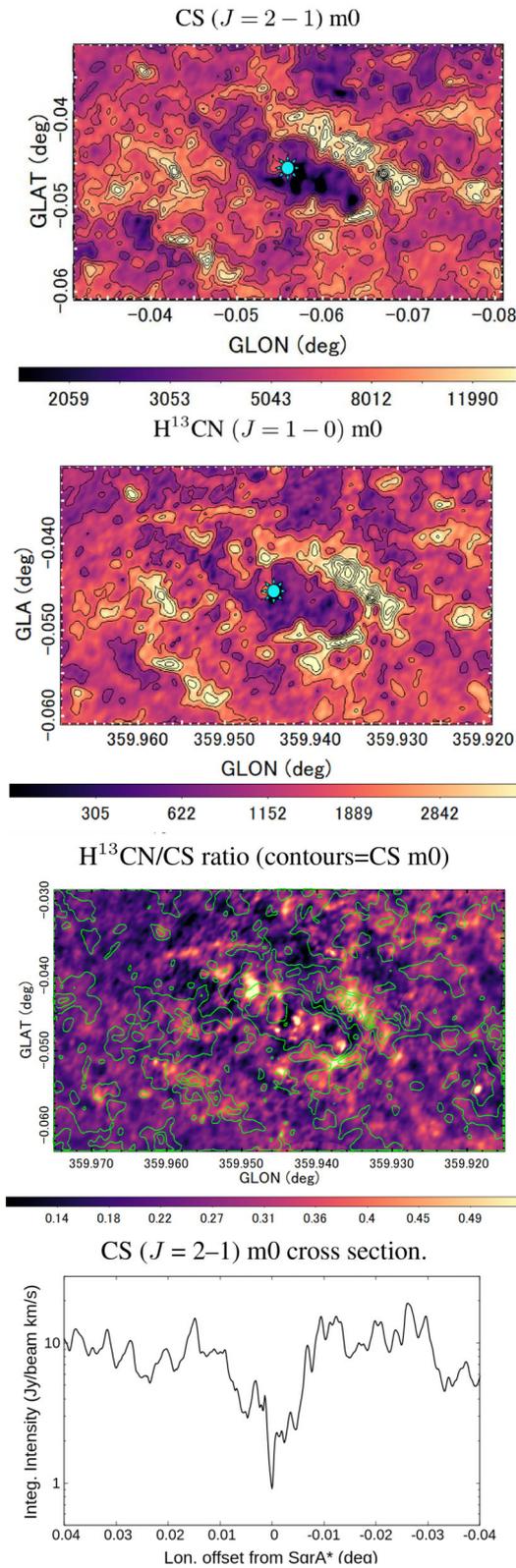
CS $(J = 2 - 1)$ m0

$H^{13}CN$ $(J = 1 - 0)$ m0

$H^{13}CN/CS$ ratio (contours=CS m0)

CS $(J = 2-1)$ m0 cross section.

Fig. 2. Close up of the moment 0 maps for the central $0°05 \times 0°03$ region centered on Sgr A∗. Note the "molecular hole" in the center. Top: CS $(J = 2 - 1)$ with contours every 2.5 Jy beam^{-1} km s^{-1}. The asterisque indicates the position of Sgr A∗ at $(l, b) = -0°055835, -0°046110)$ (Xu et al. 2022). Second: Same, but in $H^{13}CN$ $(J = 1 - 0)$ with contours every 1 Jy beam^{-1} km s^{-1}. Third: Ratio of the HCN-to-CS moment 0 maps with contours of CS every 4 mJy beam^{-1} km s^{-1}. Bottom: Longitudinal cross-section in CS $(J = 2 - 1)$ line showing a hole of molecular gas inside $R \lesssim 1.5$ pc. The sharp negative peak at offset 0 is the absorption of the continuum emission from Sgr A∗.

explained by the model of a rotating disk in the spherical potential (figure 4). Note that the hole is visible in the model for the spherical potential but not for the disk and bar potentials.

It is important to emphasize that, as shown in figure 2 observationally, both a possibly optically thick CS $(J = 2 - 1)$ and an optically thin $H^{13}CN$ $(J = 1 - 0)$ line show the central hole. The hole must be real and exist independently of the opacity of the molecular line considered; even CS $(J = 2-1)$ becomes invisible there.

2.5 The minispiral

The minispiral is composed of high-speed flows of ionized gas orbiting the central supermassive black hole (SMBH) drawing three elliptical orbits with Sgr A∗ being the common focal point (Tsuboi et al. 2017; Zhao et al. 2009). Their trajectories in the PV plane provide useful kinematical information about the gravitational potential.

Figure 5 (top and second panels) shows the moment 0 map in H40α of the minispiral and superposition with that in CS. The north-west arms in H40α and CS apparently overlap, but are separate arms as shown by the 3D LBV projection below. The third panel shows a superposition of the LVDs. The terminal velocity in the CS line is partially connected to the high-velocity envelope in H40α, which increases toward the nucleus. The envelope velocity is approximately presented by the Keplerian law for a point mass of $4 \times 10 \, M_\odot$ at the center, as indicated by the white lines in the third panel.

The fourth and fifth panels of figure 5 show oblique 3D projections of the pixel points with intensity greater than 0.175 Jy beam^{-1} from the LBV cubes in the H40α (violet) and CS $(J = 2 - 1)$ (green) lines from the longitude and latitude sides. These diagrams show that the minispiral in H40α is a separate system from the CND in phase space. The molecular gas structure of the CND is not connected to the ionized gas of the minispiral.

Figure 6 (top panel) shows the LVDs of the minispiral in H40α at three different latitudes. The second and bottom panels show a simulation of the trajectories of test particles of three clouds orbiting in the point-mass potential by LV and 3D projections. This simulation qualitatively proves that the observed high-velocity LVDs of the minispiral is explained by the Keplerian motion of the gas' rings or arms.

3 Diagnosis of the shape of gravitational potential by test-particle simulation

We examine the sphericity, oblateness, and triaxial ratios of the gravitational potential in the circumnuclear region by simulating the evolution of a molecular cloud. Compared with the moment 0 maps and PVDs of the molecular lines, we argue that a spherical potential is preferable in the CND and the disk oblateness is mild in the entire CMZ, but a strong bar may not apply.

3.1 Axial ratio of the potential

To examine the shape of the gravitational potential, it is convenient to assume the following form (Binney et al. 1991),

$$\Phi = 1/2 \, v_0^2 \ln \left[\sum (x_i/q_i)^2 \right], \tag{1}$$

where x_i are the Cartesian coordinates of the particle and $q = q_x : q_y : q_z$ gives the axial ratio of the potential. When
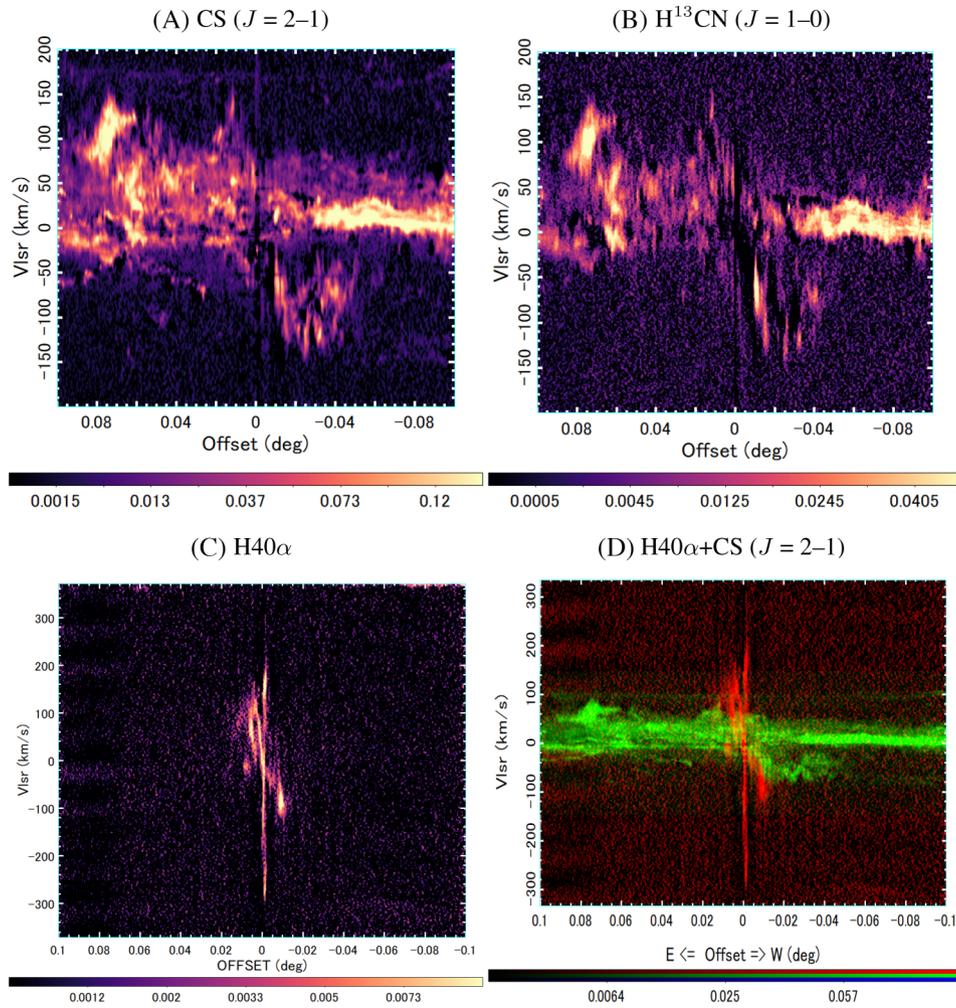
Fig. 3. (A)–(C) Position–velocity diagrams of CS ($J = 2$–1) H^{13}CN ($J = 1$–0), and H40α lines along the major axis of CND at position angle 70° (white dashed line in the top panel of figure 1) (width 10 pixels for CS, HCN, and 40 pixels for H40α). The horizontal axis is the offset from Sgr A*, positive to the east (left). (D) PVD in CS by green overlaid with H40α by red.

the potential is spherical with $q = 1 : 1 : 1$, the circular rotation velocity is constant (flat rotation). A potential with $q = 1 : 1 : q_z$ and $q_z < 1$ represents an oblate spheroid or a disk, and $1 : q_y : q_z$ with $q_y \neq q_z$ represents a triaxial bar.

In the following, the coordinates are normalized by the radius, $r = 1$, at which the circular velocity is also nomaralized to unity, $v = 1$. The cloud is represented by an ensemble of many test particles centered on the initial orbit of radius 1. The test particles are distributed in a small radius 0.1 times the orbital radius and velocity dispersion 0.1 times the orbital (rotation) velocity at the unit radius. Each test particle moves in a potential of the Galactic bulge and the cloud's gravity represented by a Plummer potential of scale radius 0.1, so that the Roche radius of the tidal force by the bulge's potential is about equal to 0.1.

3.1.1 Spherical potential–coplanar rosette orbit

Figure 7 panel A shows the result for a spherical bulge potential, showing the evolution of a cloud composed of many test particles initially placed at a radius $r_0 = (x_0, y_0, z_0) = (1, 0, 0.3)$ and circular rotation velocity $v_0 = (0, 1, 0)$, plotted every 0.1 rotation period. The cloud orbit is circular in the (x, y) plane and draws a straight line in the (x, z) plane as projected on the sky, as shown in the first (top-left) and

second charts, respectively. The LVD and BVD show straight rigid body-like behaviors, as shown in the third (bottom-right) and fourth charts.

The cloud's shape suffers from the tidal effect of the Galactic bulge and is stretched around the cloud center. It is disrupted in one orbital period and is stretched along the circular orbit, finally making a circular ring of radius 1. The projections on to the (x, z), (x, v_y), and (z, v_y) planes may be compared with the observed moment 0 map, LVD, and BVD in figures 1 and 3, and figure 20 in the Appendix. Obviously, the present simple ring model cannot reproduce the detailed properties observed in figure 1, although the elongated shape in the sky and the tilted LV and BV ridges observed in figure 1 are not inconsistent with the simulation in figure 7.

The next simplest model is a rosette orbit for a noncircular initial velocity in the spherical potential. Figure 7B shows the result for a cloud with the initial velocity oblique to the concentric circle starting from the same place as in figure 7A and traced for three orbital periods.

The (x, y) projection exhibits a rosette orbit pattern, where the cloud is disrupted within one orbital rotation and is further elongated along the orbital trajectory. The (x, z) projection, which corresponds to a projection in the sky, yields an elliptical structure with a few bifurcated arms and an empty
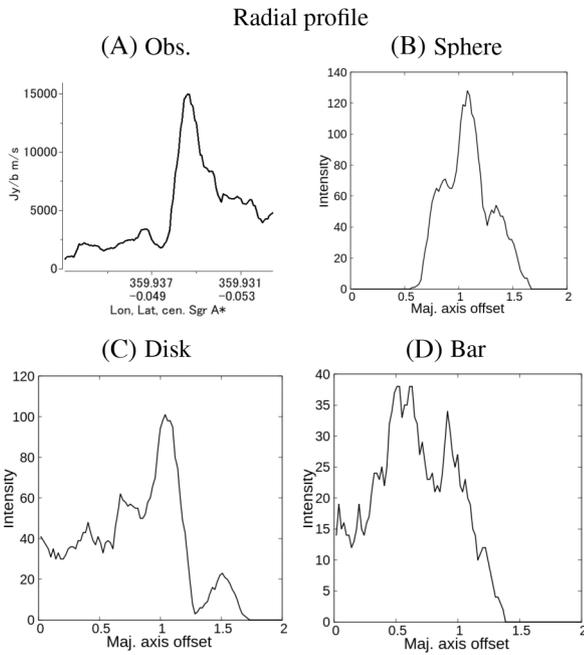
Radial profile

Fig. 4. (A) Cross-section of the moment 0 map from Sgr A* to SW at $PA = 240°$ showing a clear cut of intensity inside the CND. (B)–(D) Simulations for spherical, disk and bar potentials, respectively. The central deep hole is reproduced only by the spherical potential.

interior region, mimicking the observed moment 0 map in figure 1. We point out that the rosette orbit in the spherical potential is coplanar even if the (x, z) projection shows such an elliptical structure. In the bottom chart of figure 7B, we confirm this by a 3D projection through the orbital plane of the same simulation result.

The reason why the orbits remain in the initial coplanar plane is that the epicyclic frequencies in the horizontal (radial) and vertical directions are equal due to the spherical potential. The circumstance may also be explained by the conservation of angular momentum in the spherical potential because the gravitational force is kept always radial. The projections in the (x, v_y) and (y, v_y) planes, corresponding to LVD and BVD, respectively, also reproduce the broad tilted PV diagrams seen in figure 20 in the Appendix, although the absorbed regions are not well hidden by this simulation.

3.1.2 Disk potential

We then examine non-spherical potentials, which do not seem to explain the observations. Figure 7C shows the result of the evolution of a molecular cloud with the same initial condition as in figure 7B, but in disk potentials with $1 : 1 : 0.6$, and the evolution is traced for six orbital periods. The bottom panel is a 3D projection, demonstrating that the orbit cannot be coplanar because of the non-centrally directed force in the disk potential, which does not guarantee the angular-momentum conservation. Therefore, the (x, z) projections, corresponding to the intensity distribution on the sky, do not produce the tilted ring structure with a central hole. Comparing the result with the observations in figures 1 and 2, we conclude that a disk potential may not be a suitable approximation for the central few pc region of the Galaxy.

The reason why the orbits do not remain in the initial coplanar plane is that the epicyclic frequencies in the horizontal (radial) and vertical directions are different, so the nodal

points precede fast around the center. This is also explained by a rapid precession of the rotation axis around the Z-axis and variation of the angular momentum.

3.1.3 Bar potential

Figure 7D shows the result for the same initial condition as in figure 7B, but in bar potentials with $q = 1 : 0.8 : 0.8$. Due to the non-centrally directed force in the bar that does not guarantee the conservation of angular momentum, the orbit cannot remain in a coplanar sheet. The bar potential causes stronger precession of the rotation axis in the x-, y-, and z-axes, producing different epicyclic frequencies in the three directions and a more uniform distribution of the trajectories. Compared with the observations, we conclude that the bar potential is also not likely in the central few pc region of the Galaxy.

3.2 Constraint on the potential shape

In figure 8 we summarize the simulated results for an orbiting period of ∼10 rotations, which corresponds to ∼3 Myr at $R ∼ 3$ pc (CND). After many runs of the test particle simulations with different values of q_x and q_z, we obtained the following condition for the central potential to reproduce the observed properties of the CND. [Note that we use the CMZ or the CND as a non-self-gravitating probe to diagnose the external gravitational pontential of the Galactic bulge or the nuclear stellar cluster (NSC) and a massive black hole.]

(i) Spherical potential is preferred as the means by which the ring structure of the CND is kept flat, even though the orbits are highly eccentric (Sofue et al. 2025b). This applies also to the minispiral, each arm of which traces an ellipse, not mixed to become a 3D cloud.

(ii) In a disk potential, the angular momentum of the flow is not conserved unless the disk is perfectly parallel to the potential plane. This results in a fat disk with a thickness equal to the height of the orbit. The central hole disappears when the disk is projected in the sky because of the mixing of nodal points. The entire CMZ may be in this category. The disk potential should be sufficiently round, with $q_z \gtrsim 0.95$.

(iii) A bar potential disturbs the ring shape more strongly as a result of the angular momentum exchange. In order to keep the central hole on the sky for more than a few orbital rotations (∼ 0.1 Myr), the two axial ratios must be $q_z \gtrsim 0.95$ and $q_x \gtrsim 0.95$.

Figure 9 summarizes the final shape of the "disc" in the sphere, disk, and bar potentials. From (i) above, we conclude that the gravitational potential in the central ∼10 pc of the Galaxy is almost spherical, having an axial ratio (or ratios) greater than 0.95 to reproduce the central cavity structure of moment 0 projected on the sky and the observed LVD and BVD. This is consistent with the observed infrared luminosity distribution in the central ∼10 pc (Fritz et al. 2016; Gallego-Cano et al. 2020). From (ii) and (iii) we may also conclude that the potential containing the entire CMZ is an axisymmetric disk, or at least it is not a strong bar.

This conclusion will be used as the basis for using the rotation curve to calculate the mass distribution in the central region in the next section. We mention that the present argument applies to 3D potentials, but if the potential is assumed
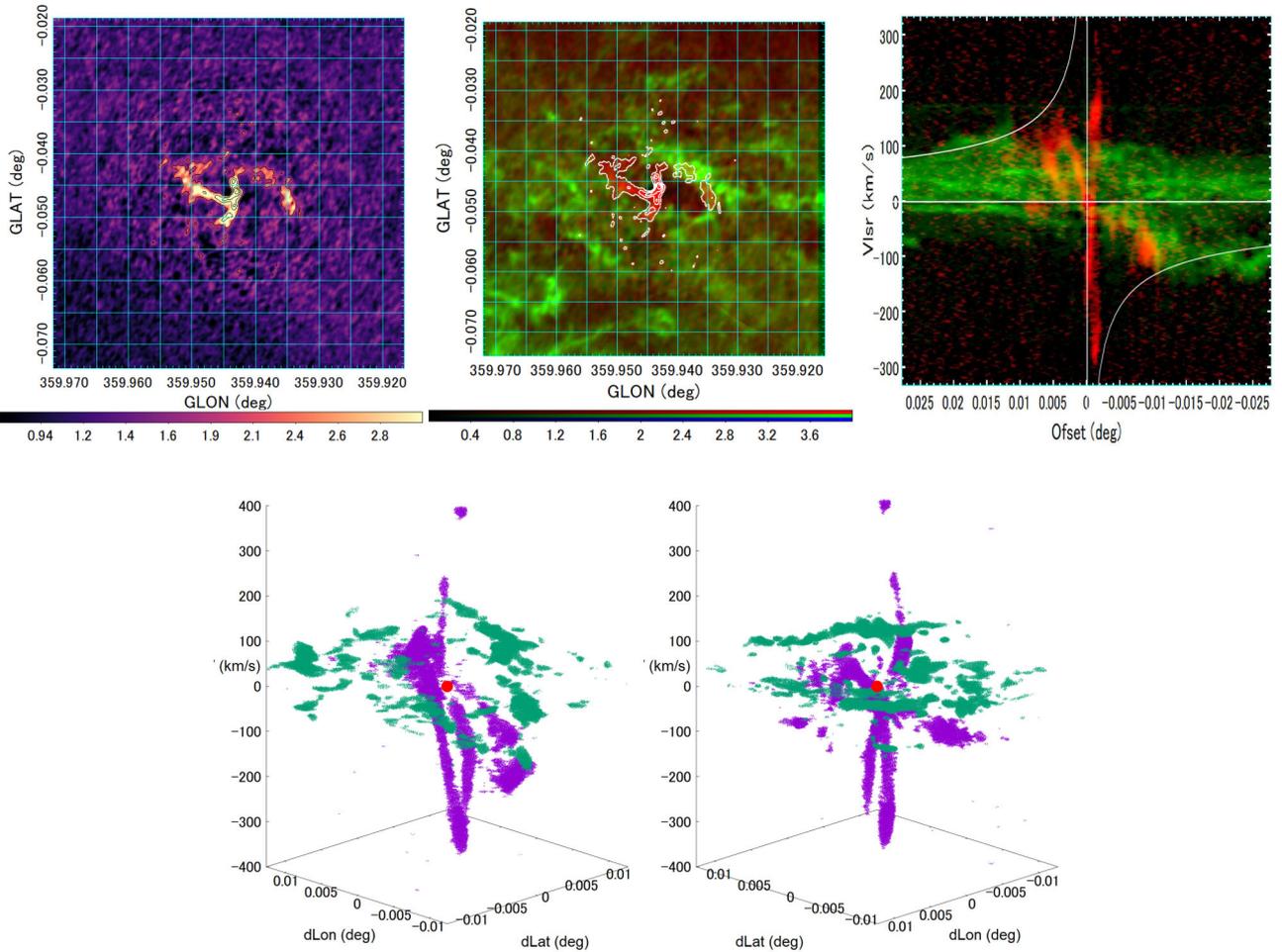
Fig. 5. Top left: Moment 0 map of the minispiral in the H40α line. Top center: Same, but with contours overlaid on the CS ($J = 2$–1) moment 0 map of the CND. Top right: Overlay of LVD of the minispiral in H40α on LVD of CND in CS ($J = 2$–1). The lines indicate a Keplerian RC for the central black hole with a mass of $4 \times 10^6\ M_\odot$. Bottom: Oblique projections of the 3D LBV H40α cube in violet from the longitude side (left) and the latitude side (right), superposed with that in the CS ($J = 2$–1) line in green.

to be 2D or axisymmetric, as employed in some simulations, the disk is kept flat by definition (no z extent).

A concern to be kept in mind is that the simulation does not take into account the gaseous properties such as the pressure and inelastic interaction between the elements. The former acts to expand the disk, whereas the latter works to the opposite. Therefore, we should consider the result to be qualitative, while the general property of the potential shape does not vary significantly.

3.3 Line profiles

In addition, the detailed shape of each line is also useful for constraining the model. The large widths of the spectral profiles are shown to manifest the kinematical properties of the gas clouds that rapidly rotate around the GC at $V_{\rm rot} \sim 100$–$150\ {\rm km\,s^{-1}}$ (Sofue et al. 2025b). Figure 10 compares the observed line profile of the eastern clump of CND with the simulated results.

The CS profile exhibits a typical lopsided and broad spectral shape typical for a receding side of a rotating disk, showing a sharp cut at the positive terminal velocity, representing the rotation velocity, and extended outskirts toward the negative velocity. The simulated profile for the coplanar rosette orbit (panel C) in the spherical potential seems better than the

others which all exhibit narrower line widths. This confirms the conclusion of the previous subsection.

4 Rotation curve of the GC

We describe the terminal velocity method using the LVDs, and apply it to the CS ($J = 2$–1) and H40α line data to obtain the rotation curve of the CMZ and CND. Based on the argument in the previous section that the central potential is nearly spherical, the rotation curve will be used to derive the mass distribution.

4.1 Terminal velocity method

The rotation curve is the most fundamental tool for measuring the mass distribution in a disk galaxy (Sofue & Rubin 2001; Sofue 2017, 2020). In this section, we apply the RC analysis to diagnose the mass distribution and potential nesting of the CMZ, which is a typical rotating disk. Among a variety of methods to measure the rotation velocity, the terminal (tangent) velocity method is the most popular and accurate for a gas disk.

The terminal velocity, $V_{\rm term}$, was measured as follows:

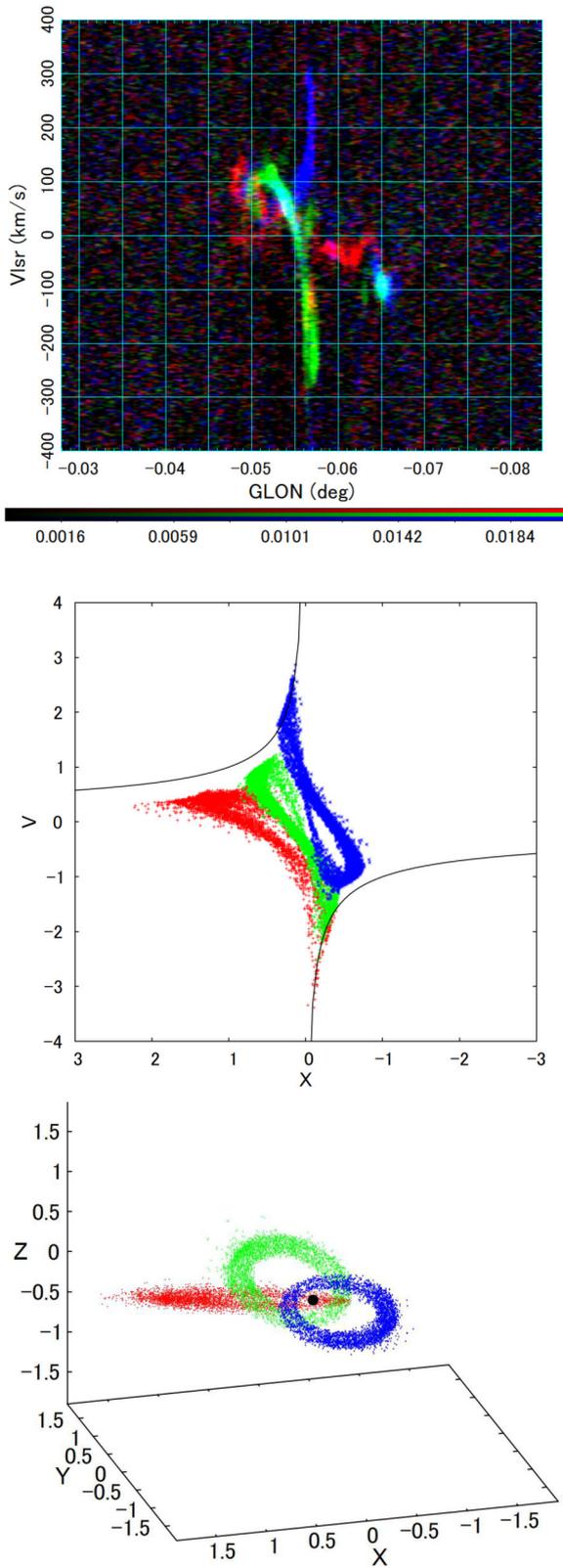Envelope trace method. A simple method applied to the H40α LVD is the envelope tracing method, which traces the

Fig. 6. Top: Overlay of LVDs in H40α of the minispiral at three different latitudes. (Middle) Simulated PVD of three clouds with arbitrary orbital parameters around a point mass projected on the (x, v_y) plane. Bottom: Same, but 3D projection.

contour drawn at a critical intensity and the errors are given half and twice the intensities of the critical intensity. The critical intensity here was taken to be three times the rms noise level.

Gaussian deconvolution of line profiles. A more precise method, which we used for the CS ($J = 2$–1) lines, is the Gaussian deconvolution of each line profile. The center velocity of the highest velocity component is taken as the terminal velocity. The line width is adopted as the standard error of the terminal velocity δV_{term}.

The absolute values of thus-determined terminal velocities are plotted as a function of the distance from Sgr A* as shown in figure 11. Finally, the raw plots of the terminal velocities are averaged in each Gaussian bin (here 0.5 pc) of the distance at every 0.5 pc to obtain a rotation curve, $V_{\mathrm{rot}}(R)$. The standard deviation of the Gaussian running average in each bin is taken as the error of RC, δV_{rot}. The rotation velocity is nearly constant at $V_{\mathrm{rot}} \simeq 120\,\mathrm{km\,s^{-1}}$ in the central several pc.

4.2 Relation of the terminal and rotation velocities

Eccentric motion is ubiquitous in the CMZ as inferred from the line-of-sight velocities of $\pm$ several tens of $\mathrm{km\,s^{-1}}$ observed at $l \sim 0°$ caused by the extended gravitational potential (Kruijssen et al. 2015; Sofue et al. 2025b). It is therefore often argued that the terminal velocity does not necessarily represent the rotation velocity due to the bar potential, where the orbit is not perfectly circular. We here argue that the terminal velocity represents the rotation velocity in case of a rapidly rotating CND.

The tangential velocity observed as the terminal velocity in the line spectrum of a gas element in an eccentric motion orbiting the Galactic potential is given by

$$V_{\mathrm{term}} = \Omega R + \kappa\, r\, \sin \kappa t, \qquad (2)$$

where $\Omega = V_{\mathrm{rot}}/R$ is the angular frequency of the Galactic rotation, and κ and r are the epicyclic frequency and radius, respectively, and t is the time. In the Galactic disk, a number of gas elements are rotating as ensembles with different epicyclic frequencies, radii, and phases. Due to the ergodic theorem, the average over the rotational behavior of many individual gas elements should result in an estimate of the rotation curve as

$$\langle V_{\mathrm{term}} \rangle = \langle \Omega R + \kappa\, r\, \sin \kappa t \rangle_t \simeq \Omega R = V_{\mathrm{rot}}(R), \qquad (3)$$

where the epicyclic term disappears in a couple of rotations or in $t \sim 0.1$–0.2 Myr. Therefore, we may safely assume that the measured V_{term} represents $V_{\mathrm{rot}}(R)$ in the present circumstances.

4.3 Rotation curves

Figure 11 shows a PVD of the H40α line near Sgr A*, showing the high-velocity motion of the minispiral. Using the envelope-tracing method, we determine the terminal velocities and plot them in the lower panel of the figure. The full line shows the Keplerian law due to the central supermassive black hole with a mass of $M_{\mathrm{BH}} = 4.2 \times 10^6 M_\odot$ (Ghez et al. 2008). The innermost terminal velocities within $R \lesssim 1$ pc fit this Keplerian motion well.

Figure 11 also shows a CS ($J = 2$–1) LVD covering the entire ACES field from $l = -0°6$ to $+0°9$ (120 pc), where the contours are drawn at $I = 0.05$ Jy beam^{-1}, approximately following the terminal velocity. The bottom panel shows the rotation curve in CS ($J = 2$–1) obtained by applying the Gaussian deconvolution method.

We then combined the H40α and CS ($J = 2$–1) rotation curves to obtain a unified RC of the CMZ, as shown in figure 12. The top panel shows the terminal velocity diagram,
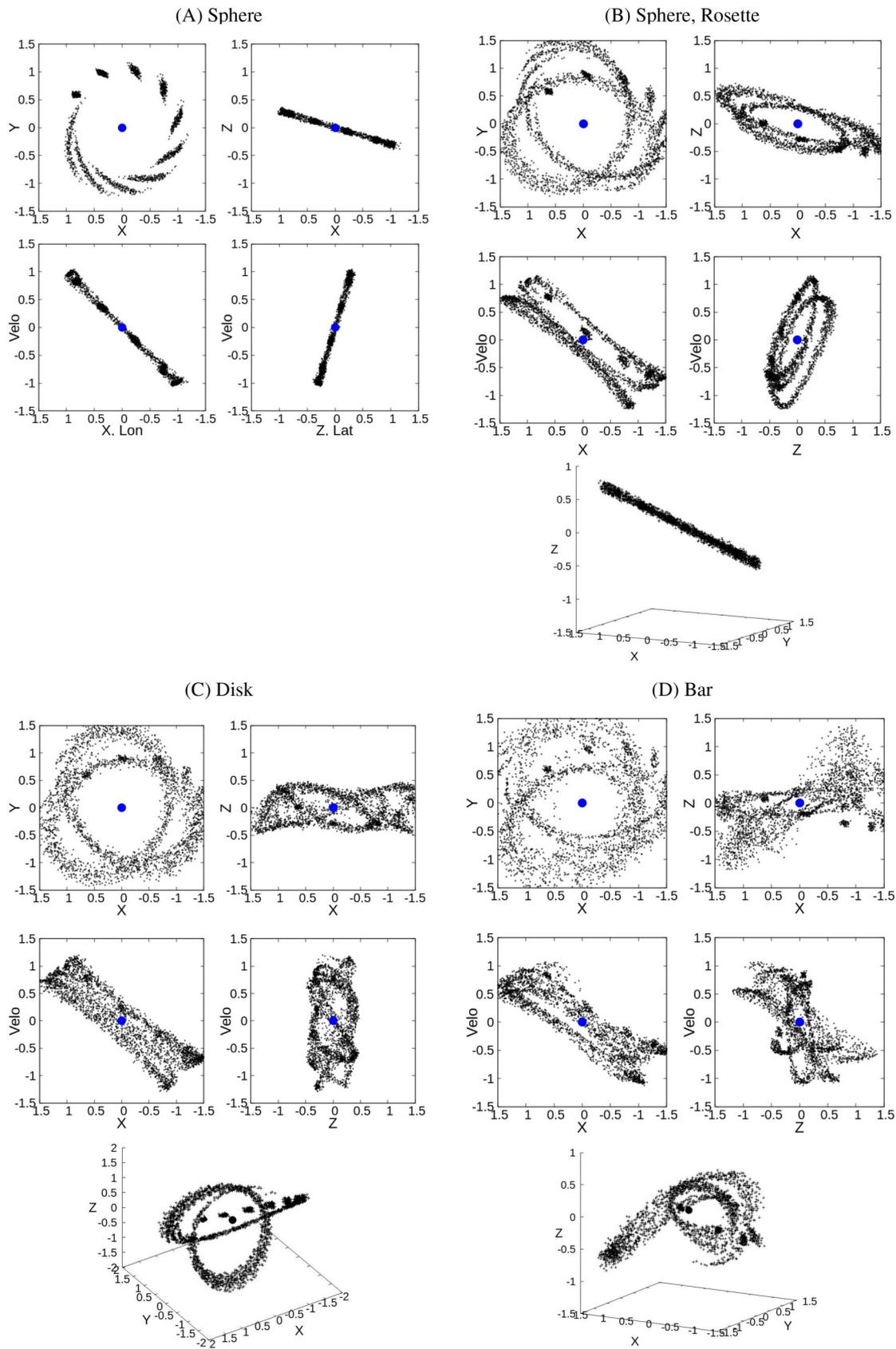
Fig. 7. (A) Circular coplanar orbit in a spherical potential with $q = 1 : 1 : 1$ starting at $(x, y, z; v_x, v_y, v_z) = (1, 0, 0.3; -0.3, 1, -0.4)$. (B) Coplanar rosette orbit in a spherical potential for $q = 1 : 1 : 1$, starting at $(1, 0, 0.3; -0.3, 1, -0.4)$. (C) Evolution of molecular cloud in disk potentials with $q = 1 : 1 : 0.6$ starting at $(x, y, z, v_x, v_y, v_z) = 1, 0, 0.3, -0.3, 1, -0.3$. (D) Non-coplanar orbits in a bar potential for $q = 0.8 : 1 : 0.8$.
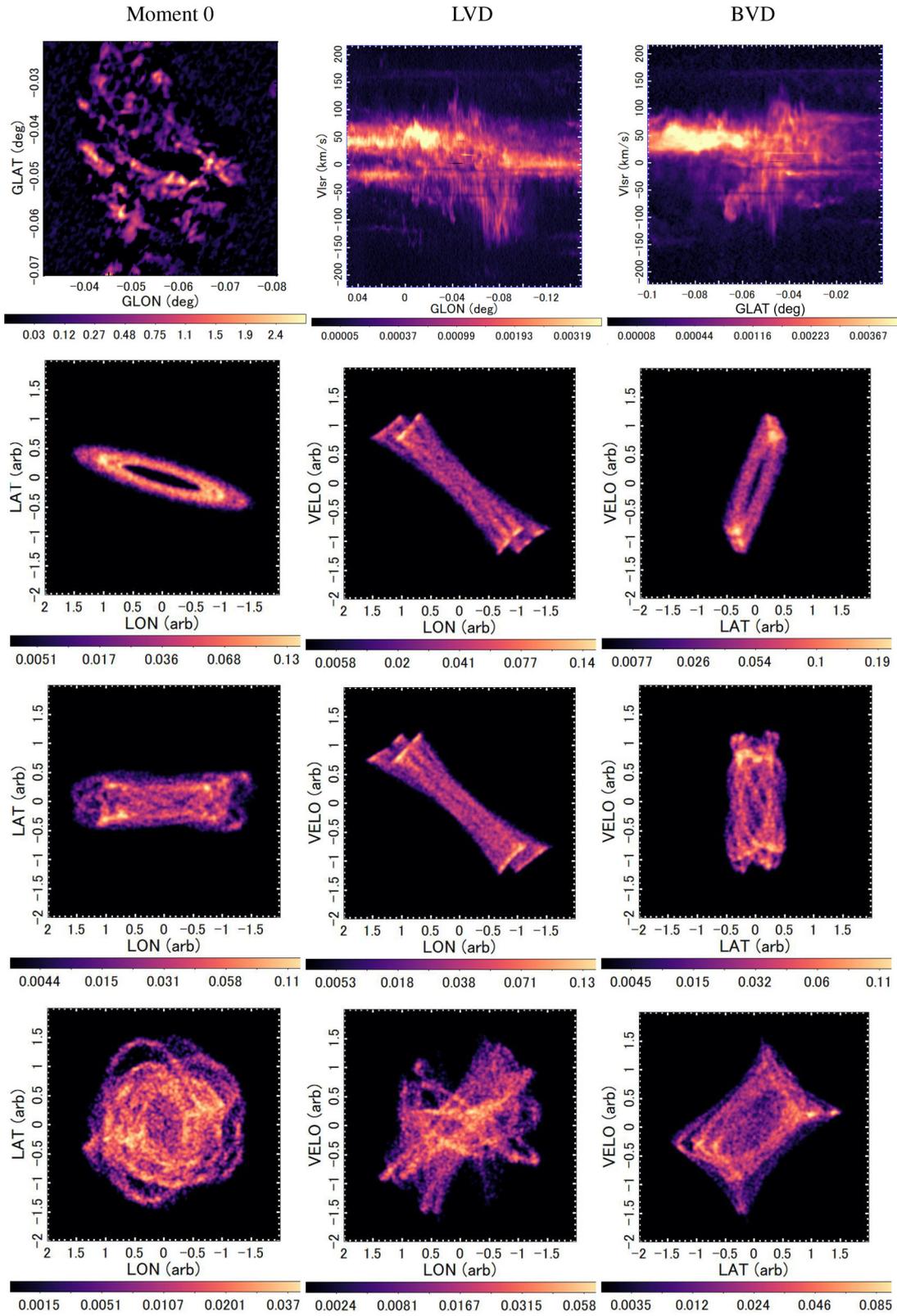
Fig. 8. Summary of the simulation compared with the observation. A spherical potential is preferred to keep the ring-shaped CND on the sky. The disk and bar strongly disturb the orbits, and the centrally holed ring totally disappears in ~0.5 Myr. Top: Observed moment 0 map in the CS line by integrating the emission along the LV ridge, LVD, and BVD. Second: Simulation in a spherical potential for ~10 rotations, reasonably reproducing the observation. Third: disk potential ($q = 1 : 1 : 0.8$) is not satisfactory to explain the observation. Bottom: Bar (1 : 0.8 : 0.8), ibid.
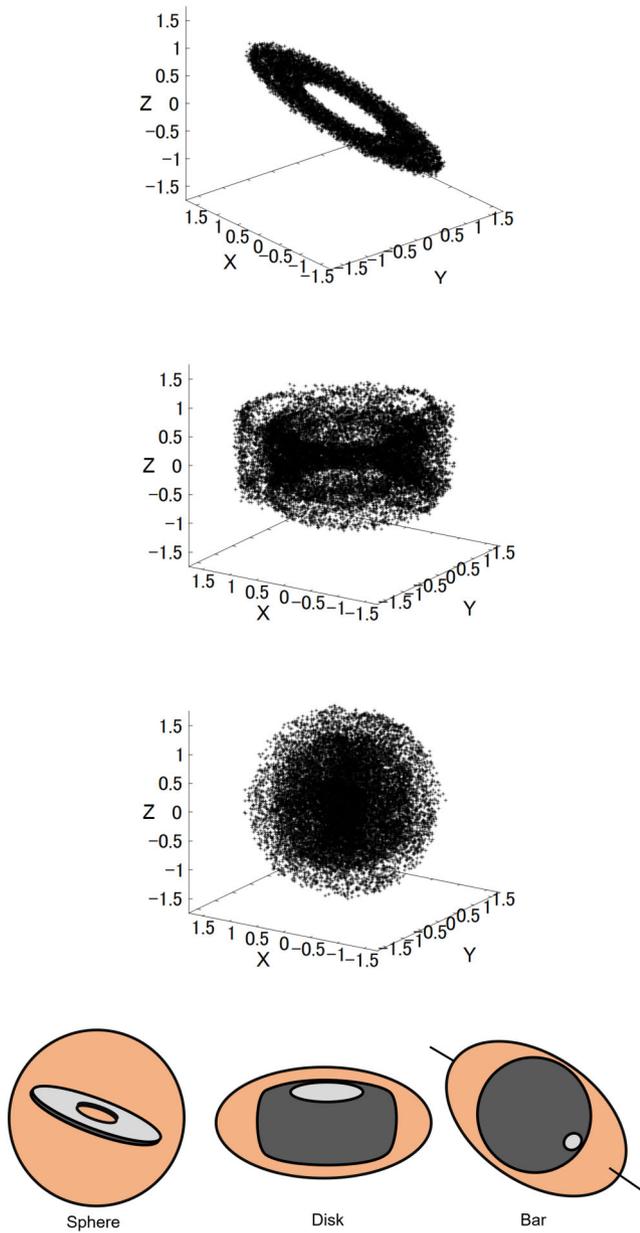
Fig. 9. Top to third: 3D plots of the test particles with initial position and velocity at $\sim (1.0, 0.0, 0.3 : 0.3, 1.0, -0.5)$ in spherical ($q = 1 : 1 : 1$), disk ($1 : 1 : 0.6$), and bar ($1 : 0.6 : 0.6$) potentials, respectively. Bottom: Schematic summary of the final 3D shape of a disk put in a spherical, disk or bar potential. "Sphere" applies to the CND orbiting in the central cluster and massive black hole, where a tilted disk or a ring can remain flat due to the conservation of angular momentum. "Disc" may apply to the entire CMZ, but (strong) "bar" may not apply in the GC.

the second shows the same but Gaussian running average has been applied, and the bottom panel shows the same in linear scaling. The rotation curve is well fitted by a superposition of two velocity components of the SMBH and the CMZ disk with a constant rotation velocity represented by

$$V_{\mathrm{BH}} = GM_{\mathrm{BH}}/R = 131.1 \ \mathrm{km\,s^{-1}}/\sqrt{X} \tag{4}$$

and

$$V_{\mathrm{CMZ}} \simeq 100 \ \mathrm{km\,s^{-1}} X/\sqrt{1 + X^2}, \tag{5}$$
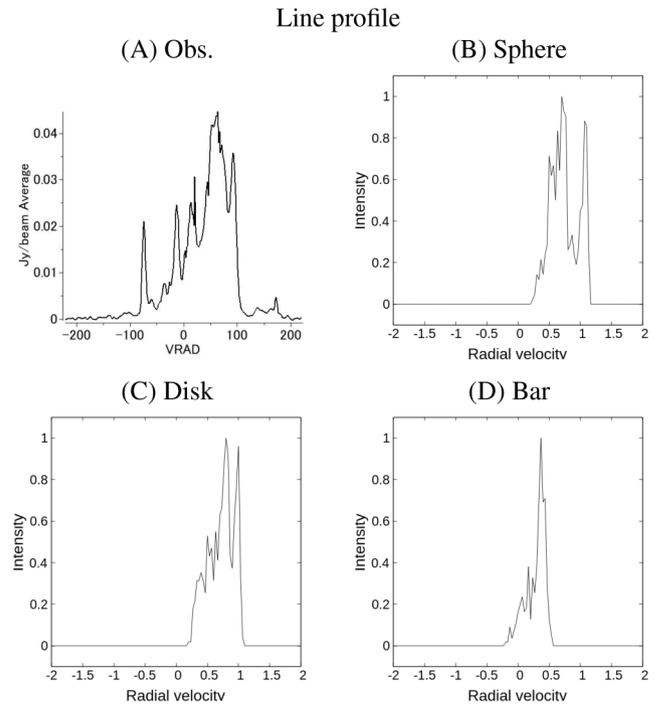
Fig. 10. (A) CS ($J = 2$–1) line spectrum of the eastern arm of CND. (B)–(D) Simulated profile for the spherical potential, disk, and bar, respectively.

which is equivalent to a potential given by

$$\Phi(X) = 1/2 v_0^2 \log \left(1 + X^2\right). \tag{6}$$

The rotation velocity is given by

$$V_{\mathrm{rot}} = \sqrt{V_{\mathrm{BH}}^2 + V_{\mathrm{CMZ}}^2}, \tag{7}$$

where $X = R/1 \ \mathrm{pc}$ and $M_{\mathrm{BH}} = 4 \times 10^6 \ M_\odot$ (Ghez et al. 2008).

4.4 Flat rotation at $V_{\mathrm{rot}} \sim 100 \ \mathrm{km\,s^{-1}}$

The rotation curve obtained in this study (figure 11) shows that the rotation is nearly flat in the CMZ at $V_{\mathrm{rot}} = 99 \pm 13 \ \mathrm{km\,s^{-1}}$. This velocity may be compared with the transverse velocity dispersion of the nuclear stellar disk of the order of $\sim 100 \ \mathrm{km\,s^{-1}}$ inferred from proper motions of the nuclear red clump stars (Nogueras-Lara 2022).

5 Mass distribution

Using the rotation curve and assuming that the gravitational potential is nearly spherical, we derive the mass distribution in the GC.

5.1 Mass, density and surface density by spherical assumption

We infer from the test particle simulations that the morphological and kinematical properties of the CND are reasonably explained by a gas flow orbiting in a spherical potential and drawing a coplanar rosette pattern. Non-spherical gravitational potentials due to a disk or a bar cannot reproduce the observed molecular-line morphology in the sky. On the basis of this result, we discuss the mass distribution in the circumnuclear region by using the rotation curve. Given the spherical
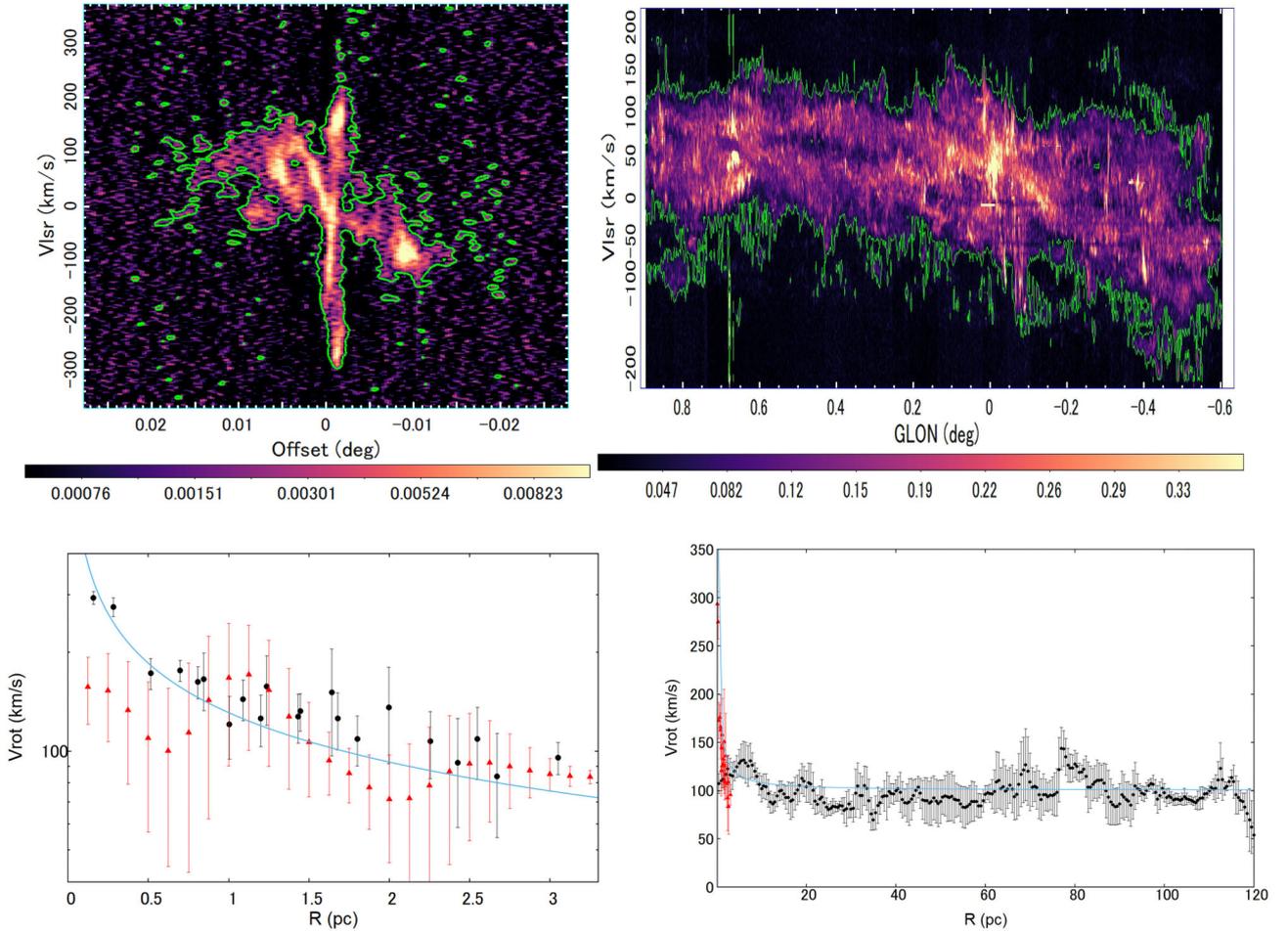
Fig. 11. Top: Position–velocity diagrams of H40α and CS ($J = 2$–1) lines at position angle 70° with a contour at several rms noise to approximately trace the terminal velocities. Bottom left: Rotation curve (terminal velocity) of the minispiral using PVDs in the top panel. Triangles and dots are obtained by the Gaussian deconvolution and envelope tracing method, respectively, while we adopt the latter. The straight line represent a Keplerian motion around the Sgr A*. Bottom right: RC in the CMZ derived by CS ($J = 2$–1) LVD by Gaussian deconvolution.

potential, the rotation curve of the central bulge is obtained using the terminal velocity along the Galactic plane.

On larger scales, infrared surface photometry indicates that the scale radii of the luminosity profile in the longitude and latitude directions are of the order of ∼0.5 at $R \sim 50$–100 pc (Schödel et al. 2014). So, even on a larger scale, such as in the bulge, the photometric shape is mild, showing a fat disk. Considering the long-range gravitational force, this means that the gravitational potential is nearly spherical in the central ∼100 pc.

In this section, we try to determine the enclosed mass within a radius R using the rotation curve obtained in the previous section, assuming that the potential is spherical, and derive the distributions of mass, density, and surface density in the GC.

The mass within R is assumed to be given by

$$M(R) = RV_{\mathrm{rot}}^2/G. \tag{8}$$

The volume density is calculated by

$$\rho_{\mathrm{dyn}}(R) = 1/\left(4\pi R^2\right) dM(R)/dR, \tag{9}$$

and the surface density is obtained by

$$\Sigma(R) = 2\int_0^\infty \rho_{\mathrm{dyn}}\left(\sqrt{z^2 + R^2}\right) dz, \tag{10}$$

or approximately

$$\Sigma(R) \sim M(R)/\left(\pi R^2\right), \tag{11}$$

where R is the GC distance in the Galactic plane and z is the height from the plane at radius R.

Figure 13 shows the calculated distributions of the total mass, volume density and surface density, using equations (8), (9), and (11), respectively. The total mass distribution is consistent with the current photometric measurements of the circumnuclear stellar cluster (CNS) and the central bulge in infrared emissions shown by the thick (green) line as plotted for comparison from the literature (Fritz et al. 2016; Gallego-Cano et al. 2020). It also smoothly continued to the Galactic dynamical mass distribution calculated for the inner RC of the Milky Way, plotted by triangles (Sofue & Kohno 2025). The red line represents the mass distribution calculated for the model RC given by equation (7). The middle panel shows the density distribution calculated using the integrated mass in the top panel. The least-squares fit to the log–log plot yields

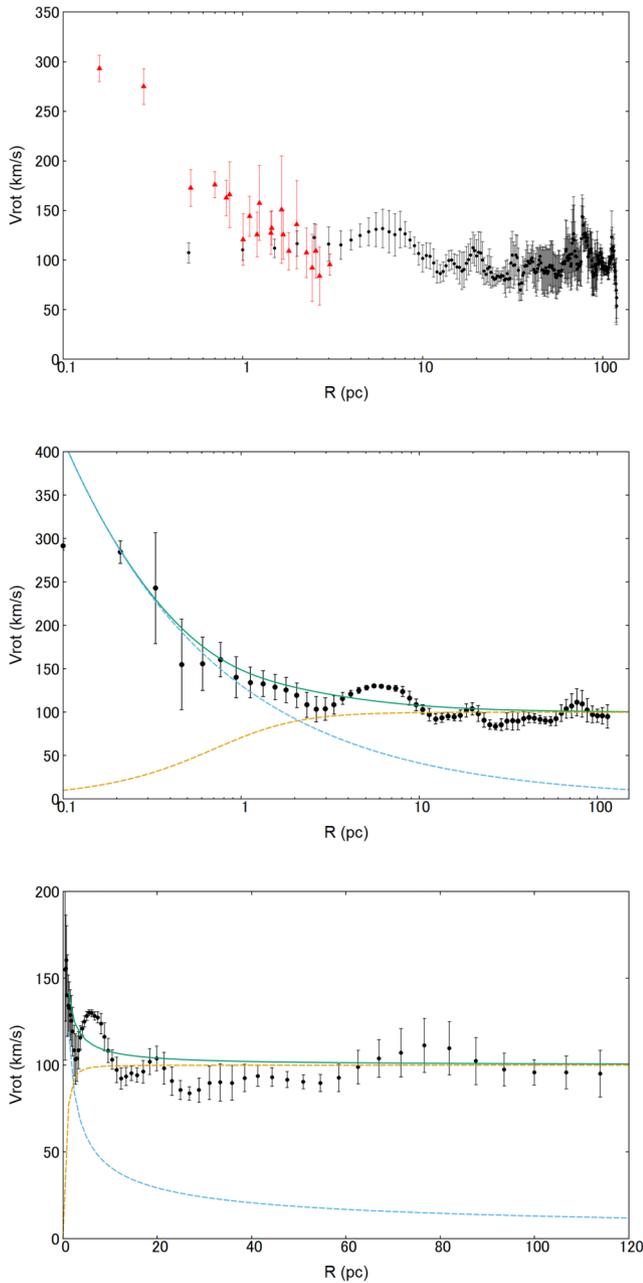$$\rho = 10^{5.194\pm0.122} \, (R/1\,\mathrm{pc})^{-1.904\pm0.090}. \tag{12}$$

Fig. 12. Top: H40α (triangles) + CS ($J = 2$–1) (dots) line terminal velocity curve (rotation curve) of the CMZ in semi-logarithmic scaling. Middle: RC after performing averaging. Bottom: Same, but in linear scaling. The curve represents calculated $V_{\rm rot}$ using equations (4) to (7).

The bottom panel shows the surface density calculated approximately using equation (11) compared with the infrared photometric measurements (Fritz et al. 2016).

5.2 Comparison with model potentials assumed in the simulations

There are two basic models to represent the central gravitational potential: the cusp type and the finite-density type.

An example of a cusp ($\Phi \sim \log R$) type assumes a potential of the form given by equation (1), which produces a constant circular velocity (flat RC) and a cuspy profile of the
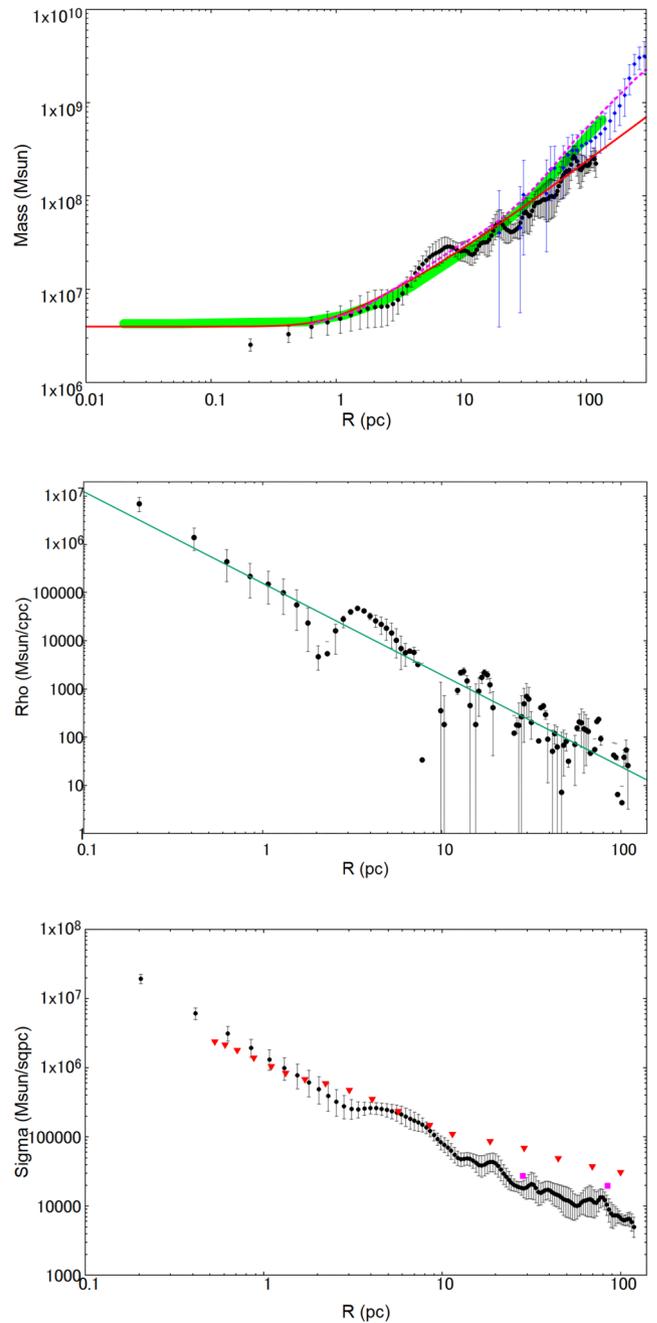
Fig. 13. Top: Enclosed mass $M(R)$ calculated for the RC in figure 11 (black dots). Measurements from the literature are summarized by Fritz et al. (2016), falling along the green thick line. The mass distribution for the innermost rotation curve is plotted by diamonds (Sofue & Kohno 2025). The dotted line is the cusp-type model No. 2 + nuclear cluster of the theoretical models by Sormani et al. (2020). Middle: Volume mass density $\rho_{\rm mass}$ calculated for $M(R)$. The straight line is a least-squares fit to the plot with equal weighting as given by equation (12). Bottom: Surface mass density $\Sigma_{\rm mass}$ approximately calculated using equation (11) compared with the infrared photometric measurement (Fritz et al. 2016).

central density as $\rho \propto R^{-2}$ (Dale et al. 2019; Kruijssen et al. 2019).

The finite-density type includes the Plummer potential and exponential, de Vaucouleurs, and/or Sersic-type density profiles (Ridley et al. 2017, and the articles cited in section 1). This type of potential yields a mild and finite density at the nucleus. The rotation velocity is zero
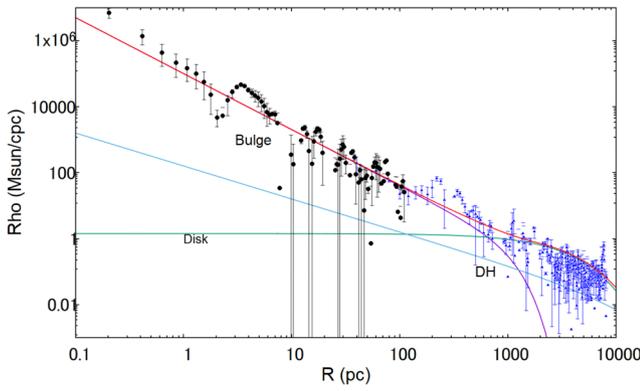
Fig. 14. Derived mass density distribution (dots) compared with the cusp-type potential used in the hydrodynamical simulation (Ridley et al. 2017). Small triangles are the density distribution in the Milky Way (Sofue & Kohno 2025).

at the center and increases linearly with radius, showing a rigid-body RC.

Figure 14 shows the comparison of the observed distribution of the dynamical mass inside the CMZ with the theoretical models adopted in the current simulations (McMillan 2017; Ridley et al. 2017). The dots are plots as calculated in this paper using the observed rotation curve. In terms of the comparison here concerned, the cusp model ($\rho \propto R^{-1}$) seems preferable to represent the potential in the central region of the CMZ.

6 Stability of the rotating gas disk in the derived potential

Using the rotation curve and potential, we argue that the gas disk is dynamically stable against star formation in the central ~ 10 pc.

6.1 Tidal enhancement vs. suppression of star formation

A rotating gas disk in the Galactic gravitational potential suffers from various external forces that either compress the gas and enhance star formation or dilute it to suppress star formation.

Various origins of protostellar clumps are proposed, such as gravitational instability in a uniform medium with small perturbations, external compression by galactic shock waves, compressing trigger by explosive events, or cloud–cloud collision. However, regardless of the origin of a gas clump, the final decision for the clump to become a "proto-stellar cloud" depends simply on the gravitational stability of the clump and on whether the self-gravitational force exceeds the thermal pressure and external disturbances. This stability is most commonly examined by the Jeans criterion. It is stressed that the Jeans instability gives the necessary condition for the clump to grow to a star. On the other hand, the Jeans stability is a sufficient condition to prevent the clump from forming a star.

6.2 Tidal disruption of a cloud

We study the tidal effect of the Galactic potential on a molecular cloud by performing an order-of-magnitude estimation.

The Roche radius for an object of mass m orbiting in the potential is given by

$$r \sim [m/M(R)]^{1/3} R. \tag{13}$$

In the case of a molecular cloud of mass $m \sim 10^4 M_\odot$ located at $R \sim 3$ pc, for example, the Roche radius is $r \sim 0.5$ pc and the critical density is $\sim 2 \times 10^4$ H_2 cm^{-3}. In figure 7 we show the evolution of the tidal deformation and disruption of a cloud orbiting at $R = 3$ pc, which initially was given a radius $r = 0.1 R = 0.3$ pc and a velocity dispersion $\sigma_v = 0.1 V_{rot} = 10$ km s^{-1} representing a cloud of mass $m = r\sigma_v^2/G \sim 0.7 \times 10^4 M_\odot$ and $n_{H_2} \sim 10^3$ H_2 cm^{-3}. The simulation reveals that a cloud is easily stretched and destroyed in the deep potential.

6.3 Tidal-Jeans (TJ) instability

The Jeans length and mass of a proto-stellar molecular cloud formed in a gas cloud of density $\rho \sim 10^5$ H_2 cm^{-3} are of the order of $\lambda_J \sim 0.1$ pc and $M_J \sim 1 M_\odot$. However, the tidal force due to the central bulge suppresses its growth. This is simply because the orbital period in the background potential is shorter than the Jeans time in the cloud. This is equivalent to the comparison of the Roche radius to the Jeans length, or to the Coriolis force stronger than the self-gravitational force.

We here discuss a modification of the linear gravitational instability of a molecular cloud using the dispersion relation for the Jeans criterion in a rotating system (Chandrasekhar 1954, 1961), which is written as

$$\omega^2 = c_s^2 k^2 - 4\pi G\rho + 4\Omega^2, \tag{14}$$

where ω and k are the angular frequency and wavenumber, respectively, of the linear perturbation represented by $\delta\rho \propto \exp(\omega t - kr)$, ρ is the gas density, c_s is the sound velocity, and $\Omega = R/V_{rot} = 2\pi/t_{rot}$ is the angular velocity of the rotating system with t_{rot} being the period of rotation. This equation is equivalent to the dispersion relation taking into account the tidal effect (Jog 2013) written as

$$\omega^2 = c_s^2 k^2 - 4\pi G\rho + T, \tag{15}$$

where $T = -\partial^2\Phi/\partial r^2$ is the external tidal acceleration per unit distance and Φ is the gravitational potential in which the cloud orbits, and if the orbit is circular its angular speed is equal to Ω.

We comment that equations (14) and (15) treat the tide as purely radial (spherical), which is assumed in the present circumstance. However, if the potential is not spherical, for example a disk (Kruijssen et al. 2019), the cloud is compressed in the vertical direction by the vertical gravity of the disk and is further tidally stretched vertically, the former enhancing star formation, but the latter suppressing it.

Equation (14) yields the modified critical wavelength corresponding to $\omega^2 = 0$, which we call the tidal-Jeans (TJ) wavelength,

$$\lambda_{TJ} = 2\pi/k_{TJ} = \lambda_J \left(1 - Q_{TJ}^2\right)^{-1/2}, \tag{16}$$

where

$$Q_{TJ} = 2\Omega t_J \tag{17}$$

is a TJ Q value defined by the ratio of the free-fall time, or Jeans time, of the cloud

$$t_J = 1/\sqrt{4\pi G\rho} \tag{18}$$

to the free-fall time $t_{ff} \sim 1/\Omega$ in the external potential of the galaxy, and

$$\lambda_J = 2\pi c_s t_J \quad (19)$$

is the Jeans wavelength. The TJ mass is then given by

$$M_{TJ} = M_J \left(1 - Q_{TJ}^2\right)^{-3/2}, \quad (20)$$

where

$$M_J = (4\pi/3)\left(\lambda_J/2\right)^3 \rho. \quad (21)$$

is the Jeans mass.

When the wavelength λ and the mass M are smaller than these critical values, specifically if $\lambda < \lambda_J$ or $M < M_J$, then ω is imaginary, leading to a stable oscillation of the perturbation. Vice versa, ω is real and the perturbation grows, and the system is unstable. It is stressed that equation (16) has no solution, or the system is stable when

$$Q_{TJ} > 1, \text{ or } t_J > 1/2\Omega, \quad (22)$$

or when the Jeans time is longer than the galactic rotation period, regardless of the sound velocity or regardless of wavelength and mass. Equation (22) can be read as

$$R < R_T = 2t_J V_{rot} = 2V_{rot}/\sqrt{4\pi G\rho}, \quad (23)$$

so, the gas disk is stable within a critical radius R_T, depending on density and rotation velocity. For $V_{rot} = 120 \text{ km s}^{-1}$, we have

$$R_T \sim 14 \left(\rho/10^5 \mu H_2 \text{ cm}^{-3}\right)^{-1/2} \text{ [pc]}, \quad (24)$$

where $\mu = 1.38$ is the correction for heavy elements.

For convenience in presenting the analyzed results, we introduce the parametric wavelength λ^* and mass M^* normalized by the critical TJ values corresponding to a sound velocity of $c_s = 1 \text{ km s}^{-1}$, which are used in the plots in figure 15:

$$\lambda^*(\rho) = \lambda_{TJ}/\left(c_s/1 \text{ km s}^{-1}\right), \quad (25)$$

and

$$M^*(\rho) = M_{TJ}/\left(c_s/1 \text{ km s}^{-1}\right)^3. \quad (26)$$

6.4 TJ criterion in Keplerian potential around the SMBH

Although trivial, it is interesting to point out that the radial transition of the TJ criterion becomes more sensitive to the GC radius if we assume a steeper potential such as that by a point mass. This effect becomes critical near the central SMBH at $R \lesssim 2$ pc. In figure 16 we compare the dependency of the M_{TJ} curve between the flat rotation as discussed in this paper and that calculated for a Keplerian rotation around the SMBH. The curves are shown for five different gas densities, increasing every 10 times from the top to bottom curves for five orders of magnitude.

6.5 Toomre's stability of a rotating disc

Although essentially the same as the Jeans criterion, the stability of a self-gravitating disk in rotation has been analyzed in terms of surface density (Toomre 1964). Although an exact analysis does not apply here because the external potential is stronger, here we try to estimate the effect of the tide on the stability of the disk. The dispersion relation for an axisymmetric density perturbation in a thin disk is given by

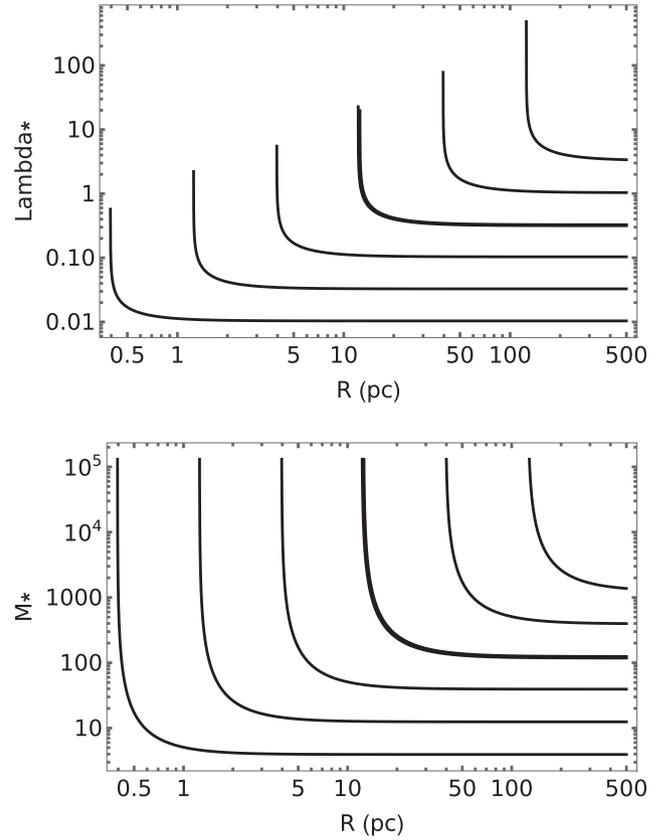$$\omega^2 = c_s^2 k^2 - 2\pi G\Sigma_g k + \kappa^2, \quad (27)$$

Fig. 15. $L_* = \lambda_{TJ}/(c_s/\text{km s}^{-1})$ (top) and $M_* = M_{TJ}/(c_s/\text{km s}^{-1})^3$ (bottom) for gas densities from $n_{H_2} = 10^3$ (top right curve) to $10^8 \mu$ (bottom left curve) H_2 cm^{-3}, with thick curve for $10^5 \mu$ H_2 cm^{-3}. Galactic rotation velocity is $V_{rot} = 120 \text{ km s}^{-1}$. Note the tilted belt covered by the strongly curved region from outer horizontal to inner vertical lines, which we call the "tidal-Jeans transition region."

where κ is the epicyclic frequency and Σ_g is the surface density of the gas disk (Binney & Tremain 2008). The critical wavelength is given by

$$\lambda_Q = 2\pi/k = \left(2c_s^2/G\Sigma_g\right)\left[1 \pm \sqrt{1 - Q^2}\right]^{-1}, \quad (28)$$

where

$$Q = c_s \kappa/\pi G\Sigma_g \quad (29)$$

is the Toomre's Q value. If $Q > 1$, equation (27) has no solution and the disk is stable (oscillation as $\propto \exp i|\omega|t$), while if $Q < 1$ the disk is unstable (growing as $\propto \exp |\omega|t$) and radially fragmented by self-gravity.

In the present case of CND, where the rotation curve is flat, we may approximate the epicyclic frequency by $\kappa \sim \sqrt{2}\Omega = \sqrt{2}V_{rot}/R$. In figure 17 we plot the Q value as a function of R for a gas density $\rho \sim 10^5$ H_2 cm^{-3}, assuming that the thickness of the disk varies as $h \sim 0.1R$, which yields $\Sigma_g = \rho h \propto R$. Figure 18 shows the same, but using the observed rotation curve for three different gas densities.

The gas disk is shown to be stable inside $R \lesssim 1.4$ pc, where $Q \geq 1$. Outside 1.4 pc, the disk is unstable and the critical wavelength of growing instability decreases with the radius, as shown in the bottom panel of figure 17.
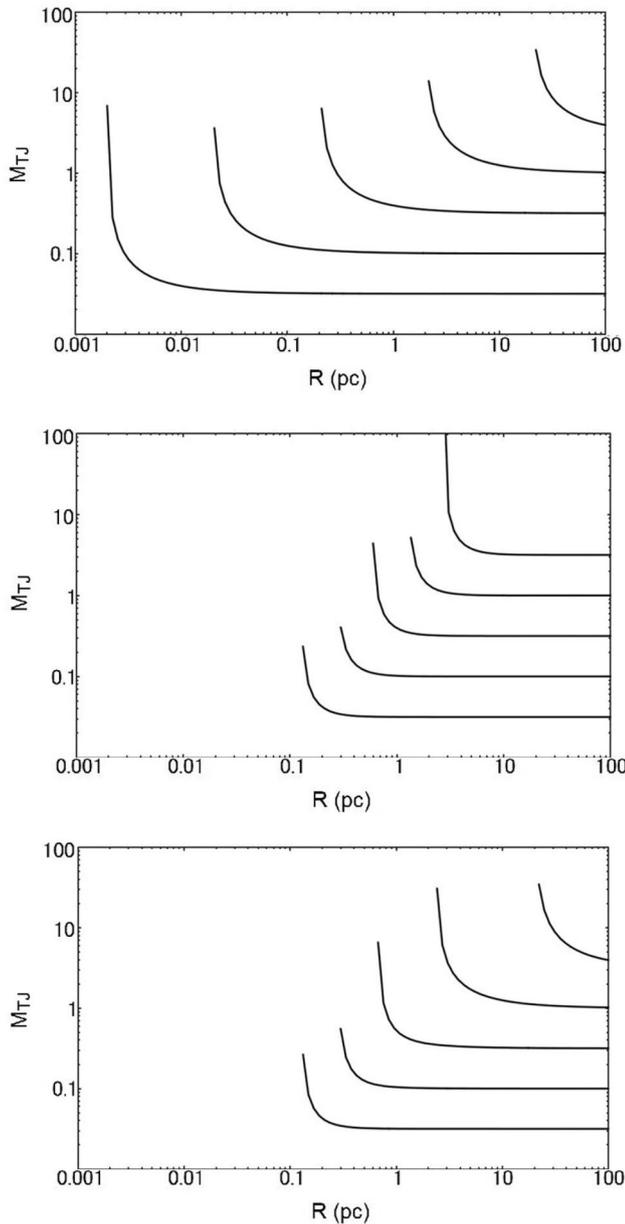
Fig. 16. Top: Normalized TJ mass of a gas cloud with density from 10^3 (uppermost curve) to 10^7 (lowermost curve) H_2 cm^{-3}, orbiting in a potential with a flat rotation curve. Middle: Same, but around a point mass with Keplerian orbit. Bottom: Same, but in a potential with a flat rotation curve superposed by a potential of a point mass.

However, we note that the Q value analysis is valid only for an infinitesimally thin disk with axisymmetric fragmentation into rings. In addition, the external potential, which is treated mixed, may act to further stabilize the disk. In fact, the calculated value of the wavelength is unreasonably small to be on the order of $\sim 10^{-3}$ pc, which is due to the assumed condition that the sound velocity is small, the disk is thin, and there are no other velocity dispersions. Furthermore, in order to discuss star formation, we need to further test the fragmentation of individual rings into proto-stellar clouds in the azimuthal direction. Therefore, we must be careful to apply it to the present circumstance, where the disk thickness is comparable to the radial extent.
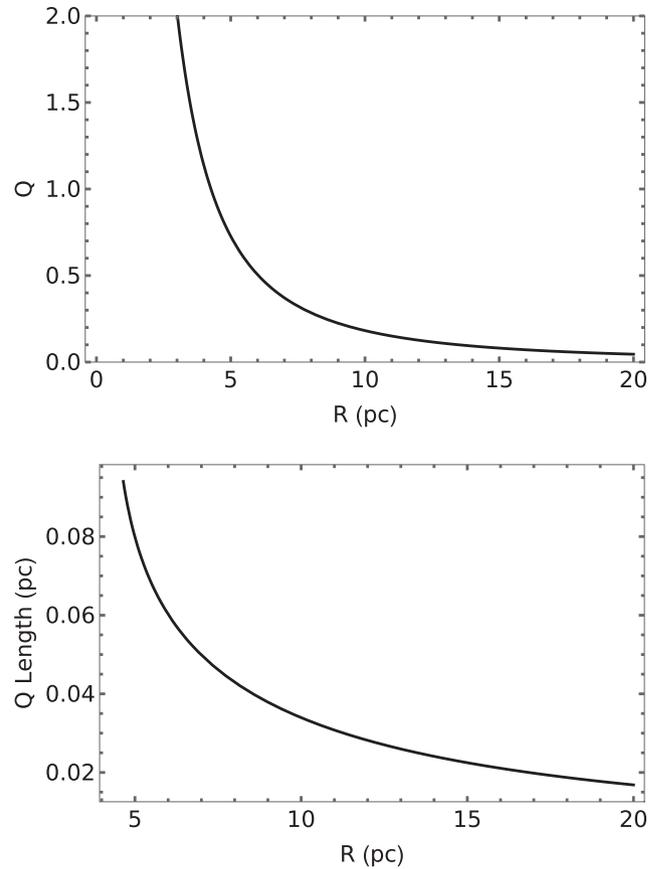
Fig. 17. Top: Toomre's Q value for a constant rotation velocity $V_{\rm rot} = 120$ km s^{-1}, $n_{H_2} = 10^5$ H_2 cm^{-3}, and $c_s = 1$ km s^{-1}, where the disk thickness is one tenth the radius, $h = 0.1R$ ($\Sigma_g = \rho h$). The disk is stable inside $R \sim 4$ pc where $Q \geq 1$ for any wavelength. Bottom: Critical wavelength λ_Q against R. The disk is stable for a wavelength below the line.

6.6 Suppression of star formation

In order to visualize the Jeans stability of a molecular cloud due to the tidal effect, we plot in figure 15 the normalized TJ length and mass, λ^* and M^*, as a function of the galactocentric distance, R, for various densities from $\rho = 10^4$ to 10^8 H_2 cm^{-3}, assuming a constant rotation velocity of $V_{\rm rot} = 120$ km s^{-1}.

The figures tell us that the density perturbation does not grow at any wavelength and mass, if the rotation period of the system is sufficiently shorter than the Jeans time, or $t_J > t_{\rm rot}$, and regardless of the sound velocity.

On the other hand, if $t_J < t_{\rm rot}$, the critical TJ length and mass tend to the Jeans wavelength and mass, and the values become dependent on the sound velocity.

For example, if we take $\rho = 10^5 \mu$ H_2 cm^{-3}, as shown by the thick line in figure 15, the gaseous system inside a critical radius of $R_T \sim 14$ pc is stable at any sound velocity. Outside of the critical radius, the system is unstable at a wavelength of $\lambda^* > 3$ pc and a mass of $M^* > 100\,M_\odot$ for $\rho = 10^5$ H_2 cm^{-3}. If the sound velocity is $c_s \sim 0.1$ km s^{-1}, clouds with a mass greater than $\sim 0.1\,M_\odot$ can grow.

We stress that the tidal suppression is effective only inside the critical radius, e.g. at $R \lesssim 14$ pc for a cloud 10^5 H_2 cm^{-3}, but outside the radius the disk stability/instability is subject to the usual Jeans criterion. In fact, a moderate or slightly higher

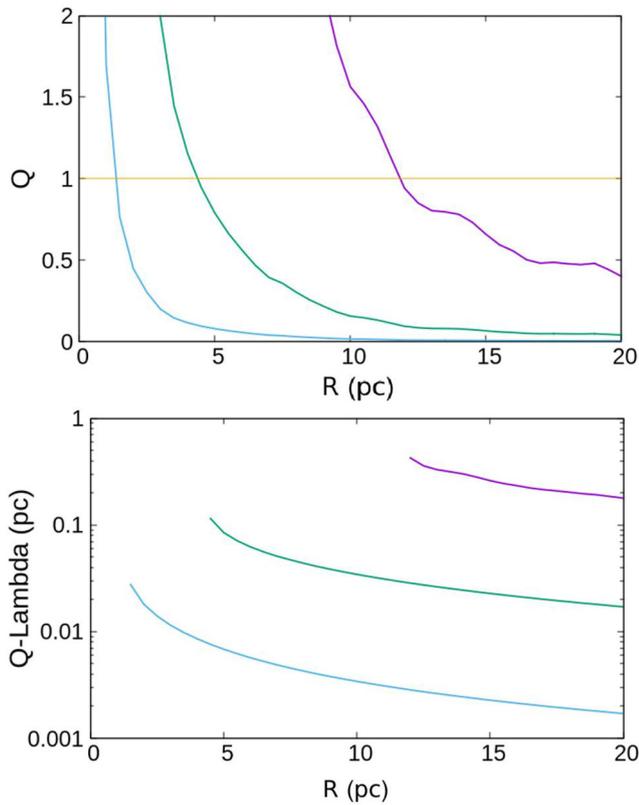**Fig. 18.** Top: Same as figure 17, but using the observed RC for $\rho = 10^4$, 10^5, and 10^6 H$_2$ cm^{-3}. Bottom: Same, but λ_Q.

Fig. 19. $L_* = \lambda_{\mathrm{TJ}}/(c_s/\mathrm{km\,s}^{-1})$ (top) and $M_* = M_{\mathrm{TJ}}/(c_s/\mathrm{km\,s}^{-1})^3$ (bottom) for gas densities from $n_{\mathrm{H}_2} = 10^4$ H$_2$ cm^{-3} (top right curve) to $10^6\mu$ H$_2$ cm^{-3} (bottom left curve) using the observed rotation curve.

star formation efficiency has been obtained in the entire CMZ (Battersby et al. 2025).

Also note that the present analysis applies to a spherical system. If a disk potential is assumed, as simulated for the mid-CMZ region (Kruijssen et al. 2019; Dale et al. 2019), the vertical tide, or the vertical gravitational force, acts to compress the cloud/disk in the vertical direction and enhances star formation.

6.7 Effect on the circumnuclear IMF

Another interesting issue is the unpredictable behavior of the tidal effect in the "transition region" in the plots λ–R and M_{TJ}–R in figures 15 and 19, where the curves suddenly turn from horizontal (outside R_{T}) to vertical (inside R_{T}). In this region, the molecular gas is neither stable nor unstable regardless of its high density. It happens that M_{TJ} varies inside a proto-cluster cloud if its size is comparable to R.

Suppose an extremely high density cloud of $\rho \sim 10^6$–10^8 H$_2$ cm^{-3} and $c_s \sim 0.1$ km s^{-1} with a size comparable to orbital radius of $R \sim 1$–10 pc; the TJ mass, which defines the cutoff mass, is variable inside the cloud from solar to high mass. This variable cut-off point for lower-mass clumps in some parts of the same cloud leads to a shallower initial mass function (IMF).

It is interesting to point out that a "top-heavy" IMF is indeed observed in the GC Arches Cluster G+0.12+0.02 (Hosek et al. 2019) and in the Quintuplet cluster G+0.15−0.05 (Hußmann et al. 2012). However, it may be less likely that these cases are explained only by tides because the clusters are located at projected distances of $\sim$25–30 pc from Sgr A*, outside the tidal transition radius.
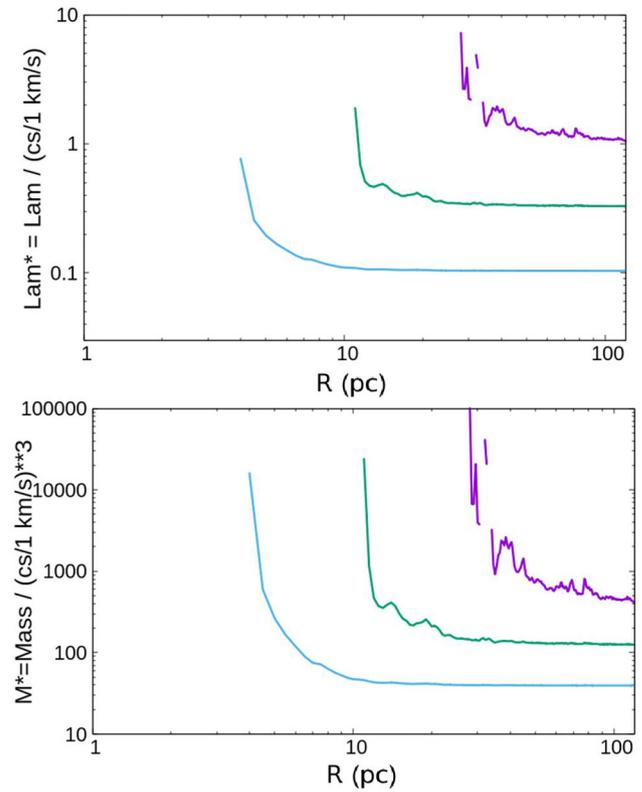
6.8 Magnetic effect

In the presence of a magnetic field B, the dispersion relation for a perturbation perpendicular to the field lines is written as (Chandrasekhar 1961)

$$\omega^2 = \left(c_s^2 + c_A^2\right) k^2 - 4\pi G\rho = 0, \tag{30}$$

where $c_A = \cos\theta B/\sqrt{4\pi\rho}$ is the Alfvén velocity, with θ being the angle between the magnetic field and the direction of contraction. This increases the critical wavelength in the direction perpendicular to the magnetic field without change of the horizontal lengths, and the critical mass increases accordingly. The magnetic strength in the GC has been measured from radio continuum observations to be $B \sim 1$ mG (Heywood et al. 2022), which yields $c_A \sim 4$ km s^{-1}, leading to a horizontal wavelength $\lambda_{\mathrm{BJ}} \sim 0.4$ pc and mass $M_{\mathrm{mag-J}} \sim 45\,M_\odot$ for $n_{\mathrm{H}_2} \sim 10^5$ H$_2$ cm^{-3}. Thus, the formation of solar-mass stars is possible from a sheet produced by an initial vertical condensation of wavelength λ_{J}, which increases the local density to cause perpendicular fragmentation of a sub-solar mass clump.

6.9 Suppression of cloud collision

Cloud collision is often argued to trigger star formation in interstellar space (Fukui et al. 2021). The collision requires a head-on orbit between the two clouds with zero angular momentum. However, a straight orbit is prohibited in the GC because of the strong Coriolis force. In the rotating disk, an object orbits around its guiding center at the epicyclic frequency $\kappa \sim \sqrt{2}\Omega$ and radius $r \sim R(\nu/\sqrt{2}V)$, with ν being the local velocity about the guiding center (velocity dispersion). Once a collision has occurred, the two clouds have had to meet re-
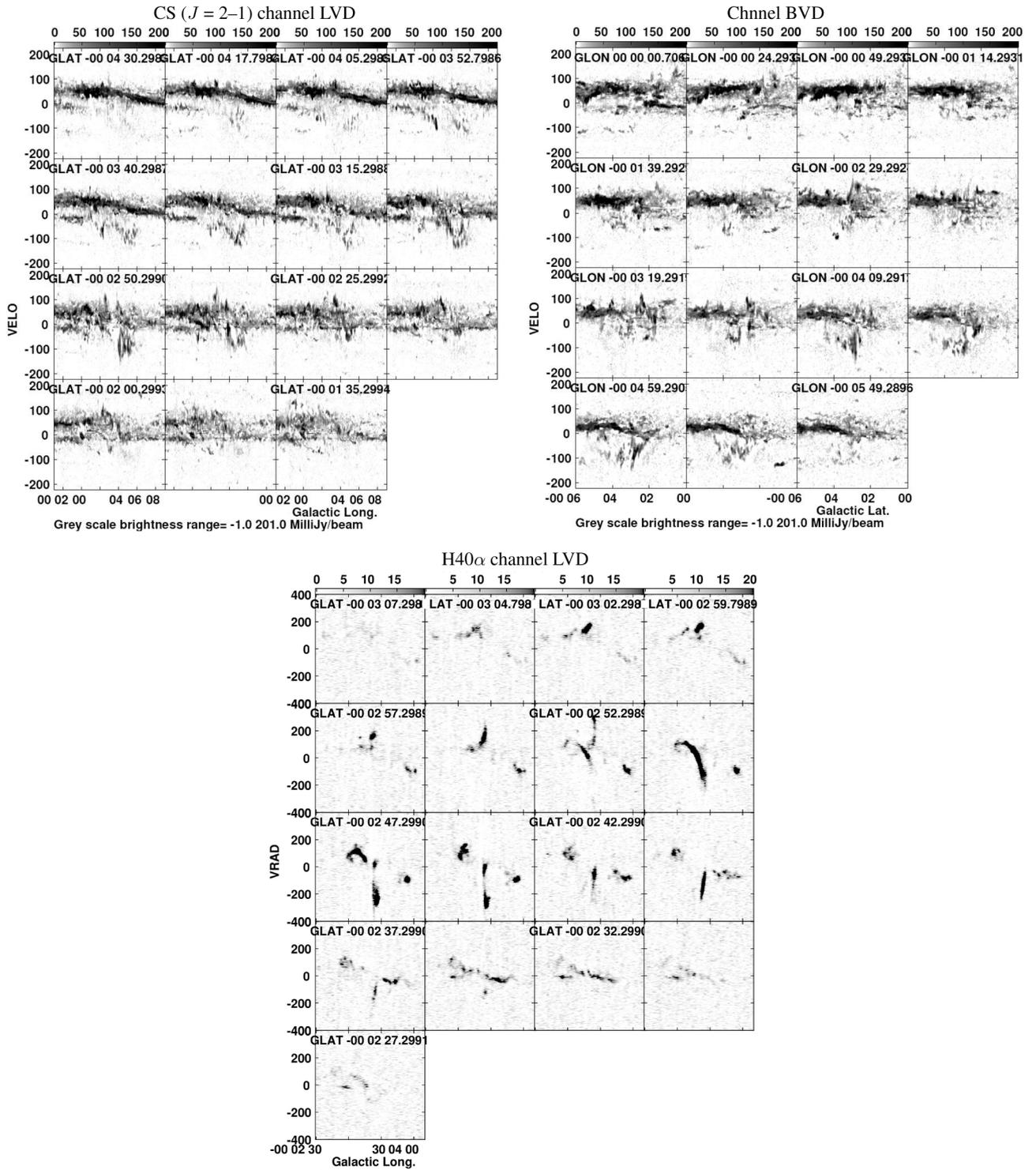
Fig. 20. Top: Channel maps of LVD (left) and BVD (right) of the circumnuclear region in the CS ($J = 2$–1) line from ACES. Bottom: Channel maps of LVD of the minispiral in the H40α line.

peatedly in the past every $t_{col} \sim t_{epi} = 2\pi/(\sqrt{2}\Omega)$. For a velocity dispersion $v \sim 20$ km s^{-1} and $R \sim 10$ pc, for example, we have $r \sim 1.2$ pc and $t_{col} \sim 0.4$ Myr. Therefore, the two clouds have been binary and the motion is a straight oscillation when they are observed in the coordinate system rotating at κ. This analysis applies to any cloud–cloud collision candidate in the Galaxy, but it is particularly serious in such a rapidly rotating disk as is considered here. Therefore, cloud collision is not an effective trigger for star formation in the GC.

6.10 Feedback from the environment

In addition to tidal and magnetic suppression of density fluctuation growth, various mechanisms are considered to act to disturb and heat the molecular gas against gravitational contraction in the central few pc of the nucleus, such as stellar winds from the extremely large number of stars inside each fluctuation, supernova explosions, and AGN activities around Sgr A*. Although these are beyond the scope of this paper, we mention that the formation of a star in the circumnuclear

region requires an extraordinarily strong mechanism to compress the protostellar gas clump.

6.11 Tidal dam toward starburst

Due to suppression of star formation, the gas that has become stagnant is trapped in the circumnuclear region, forming a super-high-density ring-shaped torus. Tidal forces act as embankments in a dam. However, when the amount of gas in the torus exceeds its limit and this dam breaks, a starburst occurs, whereas some non-gravitational compression to conquer the tide has to be activated to form a star. This is a contradictory requirement because the collision that is anticipated for shock compression is prohibited, as discussed above. Thermal instability may be a possible source of compression, although it is beyond the scope of this paper.

7 Discussion: consistency with the current works

7.1 Global vs. innermost gas dynamics

Our analysis is consistent with the current overall picture of the CMZ, but introduces new aspects regarding its more detailed structure based on the high-resolution data from ACES. In particular, the innermost dynamics and ISM conditions in the CND within $R \sim 20$ pc have been analyzed in the most detail from the perspective of galactic dynamics.

We do not specifically address the individual structures of the entire CMZ, but refer to related studies which are categorized into two models: The "twisted ellipse model" (Molinari et al. 2011; Longmore et al. 2013; Kruijssen et al. 2015; Henshaw et al. 2016; Lipman et al. 2025) and the "multi-arm model" (Sofue 1995, 2022; Sofue et al. 2025a).

The former assumes that all the named clouds (Sgr B, C, Brick, 50 and 20 km s^{-1} clouds, etc.) orbit on a single twisted eccentric trajectory at $R \sim 45$ to 130 pc. The latter assumes several arms in the framework of the density wave theory, where Arms I and II compose the 120 pc ring and Arms III to VI are inside arms. The 20 and 50 km s^{-1} clouds belong to III and V at $R \sim 40$ and ~ 10 pc, respectively, as measured using the dv/dl method on the LVDs.

However, since we use the terminal velocities (rotation curve) measured on the LVDs, the result depends little on the models.

7.2 Rotation and gravitational potential

The mass distribution derived using the rotation curve is consistent with current photometric measurements (figure 13). The gravitational potential at $R \lesssim 20$ pc favors the cusp-shaped density profile as $\propto R^{-2}$ with flat rotation as used in Binney et al. (1991). Figure 14 demonstrates this, comparing the cusp-type density model adopted in the hydrodynamical simulation of the CMZ by Ridley et al. (2017) with the present ACES result.

7.3 CND stability and low star formation efficiency

The tidal stability analysis supports the recent detailed analysis of the CND using ALMA observations by Hsieh et al. (2021), who report that half of the CND's total gas mass is capable of star formation, but no clear evidence of ongoing star formation has been found. They argue that this is because tidal forces dominate the gravitational contraction of the molecular clumps, strongly inhibiting star formation.

8 Summary

We have shown that the observed characteristics of the circumnuclear gas disk in the CS ($J = 2$–1) line are explained only when the gravitational potential of the central bulge is nearly spherical, where the rosette orbits are coplanar, but allowing for inclination from the galactic plane. We determined the rotation curve in the CMZ, which is nearly flat at $V_{\rm rot} \sim 100$ km s^{-1}, and derived the distribution of the mass, which is approximately represented by $M(R) \sim 3 \times 10^6 (R/1\,{\rm pc})\,M_\odot$ at $R \gtrsim 2$ pc. This made it possible to analyze the stability of the molecular gas in the GC using the modified Jeans instability in a rotating system. We showed that the molecular gas is stable against gravitational fragmentation for star formation in the circumnuclear region inside the threshold radius $[R \lesssim 14(\rho_{\rm gas}/10^5\,\mu{\rm H_2 cm}^{-3})^{-1/2}$ pc], where the star formation is suppressed and the SF law may be modified to have a top-heavy IMF.

Data availability

The interferometer data were taken from the ACES internal release version of the 12m+7m+TP (Total Power)-mode data from the ALMA cycle 8 Large Program "ALMA Central Molecular Zone Exploration Survey" (ACES, 2021.1.00172.L).

Acknowledgments

Appendix. LV and BV channel diagrams in the CS ($J = 2$–1) line

Channel maps of the LVD and BVD in the CS ($J = 2$–1) line are presented in figures 20.

References

Battersby, C., et al. 2025, ApJ, 984, 157

Binney, J., Gerhard, O. E., Stark, A. A., Bally, J., & Uchida, K. I. 1991, MNRAS, 252, 210

Binney, J., & Tremaine, S. 2008, Galactic Dynamics, 2nd ed.(Princeton, NJ: Princeton University Press)

Chandrasekhar, S. 1954, ApJ, 119, 7

Chandrasekhar, S. 1961, Hydrodynamic and Hydromagnetic Stability (Oxford: Clarendon)

Dale, J. E., Kruijssen, J. M. D., & Longmore, S. N. 2019, MNRAS, 486, 3307

Fritz, T. K., et al. 2016, ApJ, 821, 44

Fukui, Y., Habe, A., Inoue, T., Enokiya, R., & Tachihara, K. 2021, PASJ, 73, S1

Gallego-Cano, E., Schödel, R., Nogueras-Lara, F., Dong, H., Shahzamanian, B., Fritz, T. K., Gallego-Calvente, A. T., & Neumayer, N. 2020, A&A, 634, A71

Ginsburg, A., et al. 2025, MNRAS, submitted

Ghez, A. M., et al. 2008, ApJ, 689, 1044

GRAVITY Collaboration 2019, A&A, 625, L10

Henshaw, J. D., et al. 2016, MNRAS, 457, 2675

Henshaw, J. D., Barnes, A. T., Battersby, C., Ginsburg, A., Sormani, M. C., & Walker, D. L. 2023, in ASP Conf. Ser., 534, Protostars and Planets VII, ed. S. Inutsuka et al. (San Francisco: ASP), 83

Heywood, I., et al. 2022, ApJ, 925, 165

Hosek, M. W., Lu, J. R., Anderson, J., Najarro, F., Ghez, A. M., Morris, M. R., Clarkson, W. I., & Albers, S. M. 2019, ApJ, 870, 44

Hsieh, P.-Y., et al. 2021, ApJ, 913, 94

Hsieh, P.-Y., et al. 2025, MNRAS, submitted

Hsieh, P.-Y., Koch, P. M., Ho, P. T. P., Kim, W.-T., Tang, Y.-W., Wang, H.-H., Yen, H.-W., & Hwang, C.-Y. 2017, ApJ, 847, 3

Humire, P. K., et al. 2020, A&A, 633, A106

Hunter, G. H., et al. 2024, A&A, 692, A216

Hußmann, B., Stolte, A., Brandner, W., Gennaro, M., & Liermann, A. 2012, A&A, 540, A57

Jog, C. J. 2013, MNRAS, 434, L56

Kruijssen, J. M. D., et al. 2019, MNRAS, 484, 5734

Kruijssen, J. M. D., Dale, J. E., & Longmore, S. N. 2015, MNRAS, 447, 1059

Krumholz, M. R., Kruijssen, J. M. D., & Crocker, R. M. 2017, MNRAS, 466, 1213

Kunneriath, D., et al. 2012, A&A, 538, A127

Launhardt, R., Zylka, R., & Mezger, P. G. 2002, A&A, 384, 112

Linke, R. A., & Goldsmith, P. F. 1980, ApJ, 235, 437

Lipman, D., et al. 2025, ApJ, 984, 159

Liu, H. B., Hsieh, P.-Y., Ho, P. T. P., Su, Y.-N., Wright, M., Sun, A.-L., & Minh, Y. C. 2012, ApJ, 756, 195

Liu, S., Wang, J., Li, F., Wu, J., Zhang, Z.-Y., Li, D., Tang, N., & Zuo, P. 2023, MNRAS, 525, 4761

Longmore, S. N., et al. 2013, MNRAS, 433, L15

Longmore, S., et al. 2025, MNRAS, submitted

Lu, X., et al. 2025, MNRAS, submitted

McMillan, P. J. 2017, MNRAS, 465, 76

Mills, E. A. C., Güsten, R., Requena-Torres, M. A., & Morris, M. R. 2013, ApJ, 779, 47

Mills, E. A. C., Togi, A., & Kaufman, M. 2017, ApJ, 850, 192

Miyamoto, M., & Nagai, R. 1975, PASJ, 27, 533

Molinari, S., et al. 2011, ApJ, 735, L33

Moser, L., et al. 2017, A&A, 603, A68

Navarro, J. F., Frenk, C. S., & White, S. D. M. 1997, ApJ, 490, 493

Nishiyama, S., & Schödel, R. 2013, A&A, 549, A57

Nogueras-Lara, F. 2022, A&A, 668, L8

Oka, T., Nagai, M., Kamegai, K., & Tanaka, K. 2011, ApJ, 732, 120

Paumard, T., Maillard, J.-P., & Morris, M. 2004, A&A, 426, 81

Portail, M., Gerhard, O., Wegg, C., & Ness, M. 2017, MNRAS, 465, 1621

Ridley, M. G. L., Sormani, M. C., Treß, R. G., Magorrian, J., & Klessen, R. S. 2017, MNRAS, 469, 2251

Schödel, R., Feldmeier, A., Kunneriath, D., Stolovy, S., Neumayer, N., Amaro-Seoane, P., & Nishiyama, S. 2014, A&A, 566, A47

Shirley, Y. L. 2015, PASP, 127, 299

Sofue, Y. 1995, PASJ, 47, 527

Sofue, Y. 2017, PASJ, 69, R1

Sofue, Y. 2020, Galaxies, 8, 37

Sofue, Y. 2022, MNRAS, 516, 907

Sofue, Y., et al. 2025a, PASJ, 77, 687

Sofue, Y., et al. 2025b, PASJ, 77, L55

Sofue, Y., & Kohno, M. 2025, PASJ, 77, 1335

Sofue, Y., & Rubin, V. 2001, ARA&A, 39, 137

Sormani, M. C., Magorrian, J., Nogueras-Lara, F., Neumayer, N., Schönrich, R., Klessen, R. S., & Mastrobuono-Battisti, A. 2020, MNRAS, 499, 7

Toomre, A. 1964, ApJ, 139, 1217

Tress, R. G., Sormani, M. C., Glover, S. C. O., Klessen, R. S., Battersby, C. D., Clark, P. C., Hatchfield, H. P., & Smith, R. J. 2020, MNRAS, 499, 4455

Tsuboi, M., Kitamura, Y., Miyoshi, M., Uehara, K., Tsutsumi, T., & Miyazaki, A. 2016, PASJ, 68, L7

Tsuboi, M., Kitamura, Y., Uehara, K., Miyawaki, R., Tsutsumi, T., Miyazaki, A., & Miyoshi, M. 2017, ApJ, 842, 94

Tsuboi, M., Kitamura, Y., Uehara, K., Tsutsumi, T., Miyawaki, R., Miyoshi, M., & Miyazaki, A. 2018, PASJ, 70, 85

Walker, D. L., et al. 2025, MNRAS, submitted

Xu, S., Zhang, B., Reid, M. J., Zheng, X., Wang, G., & Jung, T. 2022, ApJ, 940, 15

Zhao, J.-H., Morris, M. R., Goss, W. M., & An, T. 2009, ApJ, 699, 186